

Article

# Subsolidus Evolution of the Magnetite-Spinel-Ulvöspinel Solid Solutions in the Kovdor Phoscorite-Carbonatite Complex, NW Russia

Gregory Yu. Ivanyuk <sup>1,2</sup>, Andrey O. Kalashnikov <sup>2,\*</sup> , Yakov A. Pakhomovsky <sup>1,2</sup>,  
Ayya V. Bazai <sup>1,2</sup>, Pavel M. Goryainov <sup>2</sup>, Julia A. Mikhailova <sup>1,2</sup>, Victor N. Yakovenchuk <sup>1,2</sup> and  
Nataly G. Konopleva <sup>1</sup>

<sup>1</sup> Kola Science Centre, Russian Academy of Sciences, 14 Fersman Street, Apatity 184209, Russia; ivanyuk@geoksc.apatity.ru (G.Y.I.); pakhom@geoksc.apatity.ru (Y.A.P.); bazai@geoksc.apatity.ru (A.V.B.); ylya\_korchak@mail.ru (J.A.M.); yakovenchuk@geoksc.apatity.ru (V.N.Y.); konoplyova55@mail.ru (N.G.K.)

<sup>2</sup> Geological Institute of Kola Science Centre, Russian Academy of Sciences, 14 Fersman Street, Apatity 184209, Russia; pgor@geoksc.apatity.ru

\* Correspondence: kalashnikov@geoksc.apatity.ru; Tel.: +7-815-557-9628

Received: 19 September 2017; Accepted: 3 November 2017; Published: 9 November 2017

**Abstract:** The Kovdor phoscorite-carbonatite ore-pipe rocks form a natural series, where apatite and magnetite first gradually increase due to the presence of earlier crystallizing forsterite in the pipe marginal zone and then decrease as a result of carbonate development in the axial zone. In all lithologies, magnetite grains contain (oxy)exsolution inclusions of comparatively earlier ilmenite group minerals and/or later spinel, and their relationship reflects the concentric zonation of the pipe. The temperature and oxygen fugacity of titanomagnetite oxy-exsolution decreases in the natural rock sequence from about 500 °C to about 300 °C and from NNO + 1 to NNO – 3 (NNO is Ni-NiO oxygen fugacity buffer), with a secondary positive maximum for vein calcite carbonatite. Exsolution spinel forms spherical grains, octahedral crystals, six-beam and eight-beam skeletal crystals co-oriented with host magnetite. The ilmenite group minerals occur as lamellae oriented along {111} and {100} planes of oxy-exsolved magnetite. The kinetics of inclusion growth depends mainly on the diffusivity of cations in magnetite: their comparatively low diffusivities in phoscorite and carbonatites of the ore-pipe internal part cause size-independent growth of exsolution inclusions; while higher diffusivities of cations in surrounding rocks, marginal forsterite-rich phoscorite and vein calcite carbonatite result in size-dependent growth of inclusions.

**Keywords:** Kovdor; phoscorite; carbonatite; titanomagnetite; exsolution; temperature; zonation

## 1. Introduction

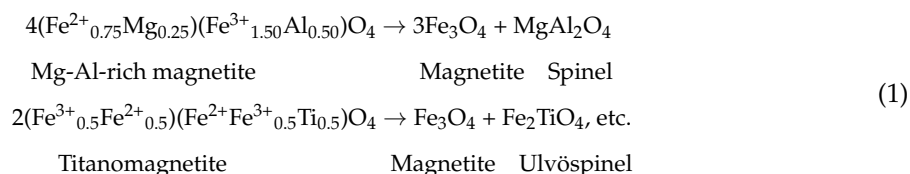
Solid solutions of magnetite  $\text{Fe}^{2+}\text{Fe}^{3+}_2\text{O}_4$  (Mag) with magnesioferrite  $\text{MgFe}^{3+}_2\text{O}_4$  (Mfr), hercynite  $\text{Fe}^{2+}\text{Al}_2\text{O}_4$  (Hc), spinel  $\text{MgAl}_2\text{O}_4$  (Spl), jacobsonite  $\text{MnFe}^{3+}_2\text{O}_4$  (Jcb), galaxite  $\text{MnAl}_2\text{O}_4$  (Glx), ulvöspinel  $\text{Fe}^{2+}_2\text{TiO}_4$  (Usp), qandilite  $\text{Mg}_2\text{TiO}_4$  (Qnd) and other members of the spinel group are of great interest because of their importance to petrology [1–16], geomagnetism [17–27], metallurgy and material sciences (ferrimagnets, electrodes, catalysts, refractories, welding materials, toners, etc.). All these minerals have a similar spinel crystal structure composed of almost cubic close-packed oxygen sublattice with cations occupying tetrahedral and octahedral interstitial sites. Normal spinellids (spinel, hercynite, galaxite, etc.) contain divalent ions in tetrahedral sites and trivalent cations in octahedral sites (Table 1). Inverse spinellids have half trivalent cations in tetrahedral positions and the balance of di- and tri-valent cations in octahedral positions (magnetite, magnesioferrite), or divalent cations in tetrahedral positions and the balance of di- and tetra-valent cations in octahedral positions

(ulvöspinel and qandilite). Besides, there are spinellids with a partially inversed crystal structure, which is especially typical for intermediate compounds, such as titanomagnetite (minerals of the magnetite–ulvöspinel series).

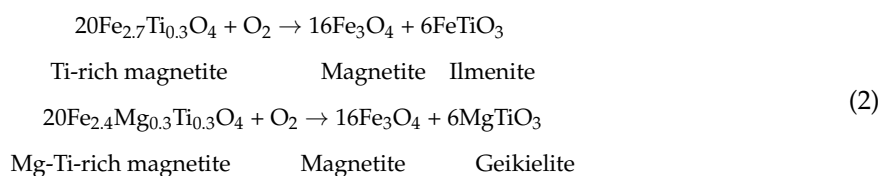
**Table 1.** Cation distribution between the tetrahedral 8f and octahedral 16c sites of the spinel structure.

Mineral	Sum of Oxides	Simplified Formula	Cation Positions		Reference
			Tetrahedral (8f)	Octahedral (16c)	
Normal spinellids					
Spinel	MgO·Al <sub>2</sub> O <sub>3</sub>	MgAl <sub>2</sub> O <sub>4</sub>	Mg <sup>2+</sup>	Al <sup>3+</sup>	[28]
Hercynite	FeO·Al <sub>2</sub> O <sub>3</sub>	FeAl <sub>2</sub> O <sub>4</sub>	Fe <sup>2+</sup>	Al <sup>3+</sup>	[29]
Galaxite	MnO·Al <sub>2</sub> O <sub>3</sub>	MnAl <sub>2</sub> O <sub>4</sub>	Mn <sup>2+</sup>	Al <sup>3+</sup>	[30]
Magnesiocoulsonite	MgO·V <sub>2</sub> O <sub>3</sub>	MgV <sub>2</sub> O <sub>4</sub>	Mg <sup>2+</sup>	V <sup>3+</sup>	[31]
Coulsonite	FeO·V <sub>2</sub> O <sub>3</sub>	FeV <sub>2</sub> O <sub>4</sub>	Fe <sup>2+</sup>	V <sup>3+</sup>	[32]
Inversed spinellids					
Magnetite	FeO·Fe <sub>2</sub> O <sub>3</sub>	Fe <sub>3</sub> O <sub>4</sub> , Fe <sup>2+</sup> Fe <sup>3+</sup> <sub>2</sub> O <sub>4</sub>	Fe <sup>3+</sup>	Fe <sup>2+</sup> , Fe <sup>3+</sup>	[33]
Magnesioferrite	MgO·Fe <sub>2</sub> O <sub>3</sub>	MgFe <sub>2</sub> O <sub>4</sub>	Fe <sup>3+</sup>	Mg <sup>2+</sup> , Fe <sup>3+</sup>	[34]
Qandilite	2MgO·TiO <sub>2</sub>	Mg <sub>2</sub> TiO <sub>4</sub>	Mg <sup>2+</sup>	Mg <sup>2+</sup> , Ti <sup>4+</sup>	[35]
Ulvöspinel	2FeO·TiO <sub>2</sub>	Fe <sub>2</sub> TiO <sub>4</sub>	Fe <sup>2+</sup>	Fe <sup>2+</sup> , Ti <sup>4+</sup>	[33]
Partially inversed spinellids					
Spinel	MgO·Al <sub>2</sub> O <sub>3</sub>	MgAl <sub>2</sub> O <sub>4</sub>	Mg <sup>2+</sup> , Al <sup>3+</sup>	Al <sup>3+</sup> , Mg <sup>2+</sup>	[36]
Magnesioferrite	MgO·Fe <sub>2</sub> O <sub>3</sub>	MgFe <sub>2</sub> O <sub>4</sub>	Fe <sup>3+</sup> , Mg <sup>2+</sup>	Fe <sup>3+</sup> , Mg <sup>2+</sup>	[34]
Jacobsite	MnO·Fe <sub>2</sub> O <sub>3</sub>	MnFe <sub>2</sub> O <sub>4</sub>	Fe <sup>3+</sup> , Mn <sup>2+</sup>	Fe <sup>3+</sup> , Mn <sup>2+</sup>	[37]
Titanomagnetite	1.2FeO·0.8Fe <sub>2</sub> O <sub>3</sub> ·0.2TiO <sub>2</sub>	Fe <sup>2+</sup> <sub>1.2</sub> Fe <sup>3+</sup> <sub>1.6</sub> Ti <sub>0.2</sub> O <sub>4</sub>	Fe <sup>3+</sup> , Fe <sup>2+</sup>	Fe <sup>2+</sup> , Fe <sup>3+</sup> , Ti <sup>4+</sup>	[33]

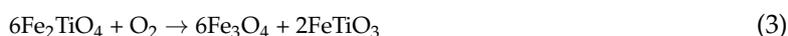
At high temperatures, complete miscibility exists between all these compounds, but at low temperatures, there are miscibility gaps between Fe<sup>3+</sup>, Al and Ti-dominant members of the spinel group. Consequently, rock cooling causes exsolution of Al and/or Ti-rich magnetite into unmixed phases whose compositions are close to their end-members, magnetite–magnesioferrite, spinel–hercynite and ulvöspinel–qandilite:



Under oxidizing conditions, titanomagnetite commonly undergoes oxy-exsolution that produces ilmenite–geikielite–pyrophanite lamellae instead of ulvöspinel–qandilite [8,38]:



Besides, exsolution ulvöspinel becomes unstable with decreasing temperature and can be oxy-exsolved at a later stage into ilmenite and magnetite [38,39]:



The Kovdor phoscorite-carbonatite complex forms a concentrically-zoned pipe-like body with gradual transition from (apatite)-forsterite phoscorite of the marginal zone to carbonate-free magnetite-rich phoscorite of the intermediate zone and carbonate-rich phoscorite and carbonatites of

the axial zone [16]. Magnetite is an accessory mineral in foidolite, diopsidite, phlogopite glimmerite and dolomite carbonatite, an accessory or minor rock-forming mineral in forsterite, apatite-forsterite phoscorite and vein calcite carbonatite and a major mineral in all other types of phoscorite and carbonatites. Its morphology, anatomy, grain size and chemical composition vary corresponding to the concentric zonation of the phoscorite-carbonatite pipe [16,40]. In addition, magnetite always contains exsolution inclusions of spinel and/or ilmenite–geikielite [40–42], providing a means to estimate the thermodynamic conditions of exsolution using the Fe–Al and Fe–Ti oxide geothermobarometers.

The results of experimental and theoretical studies [4,5,38,43–50] allowed us to estimate the equilibration temperature and oxygen fugacity of coexisting magnetite and its exsolution products based on their chemical composition. Unfortunately, we can perform only a very approximate estimation of PT-conditions of Al-rich magnetite exsolutions based on the models of magnetite-spinel miscibility [5,45]; however, Fe–Ti oxide geothermobarometers are much more informative. Most realistic results can be obtained using the model [49] calibrated with the cation-ordering data [51,52], and experimental data on  $\text{Fe}^{2+}\text{Ti} \leftrightarrow 2\text{Fe}^{3+}$  exchange between minerals of the ilmenite and spinel groups [26,53]. The model [44] can also be used for comparison.

The main objectives of the paper include studies of: (i) exsolution conditions (temperature, oxygen fugacity, cation diffusivities, etc.) of magnetite–spinel–ulvöspinel solid solution; and (ii) their dependence on rock type and spatial position within the Kovdor phoscorite-carbonatite pipe. These objectives were achieved by development and analysis of 3D-models of compositions, grain size and thermodynamic parameters of exsolution products formation.

## 2. Geological Setting

The Kovdor alkali-ultrabasic massif is situated in the SW part of the Murmansk Region, Russia (Figure 1a). It is a central-type multiphase volcano-plutonic complex of peridotite, rimmed by foidolite, melilitolite and related metasomatic rocks (diopsidite, phlogopitite, skarn-like rock and fenite) that intruded into Archean granite-gneiss 380 Ma ago. At the western contact of the diopsidized/phlogopitized peridotite core with a foidolite-melilitolite rim, a concentric zoned phoscorite-carbonatite ore-pipe ( $0.8 \times 1.3 \times > 6$  km) intrudes into the massif, forming several explosive funnels (up to 100 m in diameter) on the present-day surface (Figure 1b). Due to a steep dip of the ore-pipe wall towards its axis located in the center, the pipe diameter reduced by 40% at 600 m depth [16,54,55].

The rocks of the Kovdor phoscorite-carbonatite ore-pipe form a natural series [16,40,56], where content of apatite and magnetite first gradually increase at the expense of earliest forsterite and then decrease as a result of carbonate development in the axial zone (Figure 2). Within this series, the rocks with carbonate content over 50 modal% are called “forsterite-related carbonatite”, and the remainder of the magnetite-forsterite-apatite-carbonate rocks are called “phoscorite”. Phoscorite varieties were designated according to the main minerals [16]: C, carbonate (mainly calcite); M, magnetite; A, apatite; and F, forsterite (the respective abbreviator of a rock-forming mineral is included in denomination of a rock if the content of this mineral exceeds 10 modal %), e.g., AF (apatite-forsterite phoscorite) etc.

As a result, the phoscorite-carbonatite pipe has concentric gradual zonation (Table 2), with marginal (earlier) forsterite-rich phoscorite (A, F, AF), intermediate low-carbonate magnetite-rich phoscorite (M, MF, MA, MAF) and axial calcite-rich phoscorite and phoscorite-related carbonatite (C, CM, CA, CF, CMA, CMF, CMAF). Except for phoscorite-related carbonatite, there are later veins of calcite carbonatite (up to 3 m thick) that irregularly intersect the entire volume of the pipe and surrounding silicate rocks. Later magnetite-dolomite-(phlogopite)-serpentine rock (a metasomatite after forsterite-rich phoscorite and peridotite) constitutes the separated Eastern Satellite and several enclaves within the main ore-pipe, and a linear vertical zone of dolomite carbonatite extends from the central part of the main ore-pipe to the Eastern Satellite. Funnel-like bodies of porous breccias consisting of fragments of hydrothermally-altered phoscorite and carbonatite cemented by

colloform carbonate-rich fluorapatite (staffelite) complete the formation of the phoscorite-carbonatite complex [16,40,54,57].

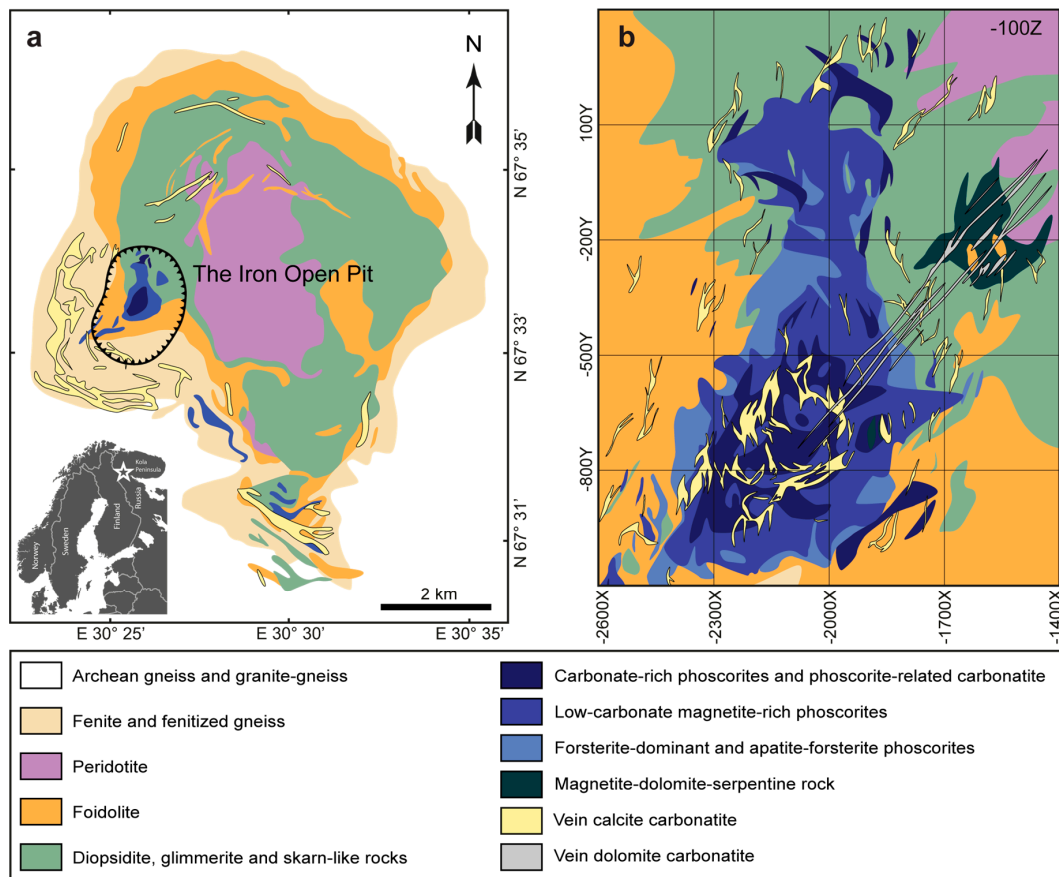


**Figure 1.** Geological maps of the Kovdor alkaline ultramafic massif (a) and phoscorite-carbonatite pipe (b) generalized on the basis of [40].

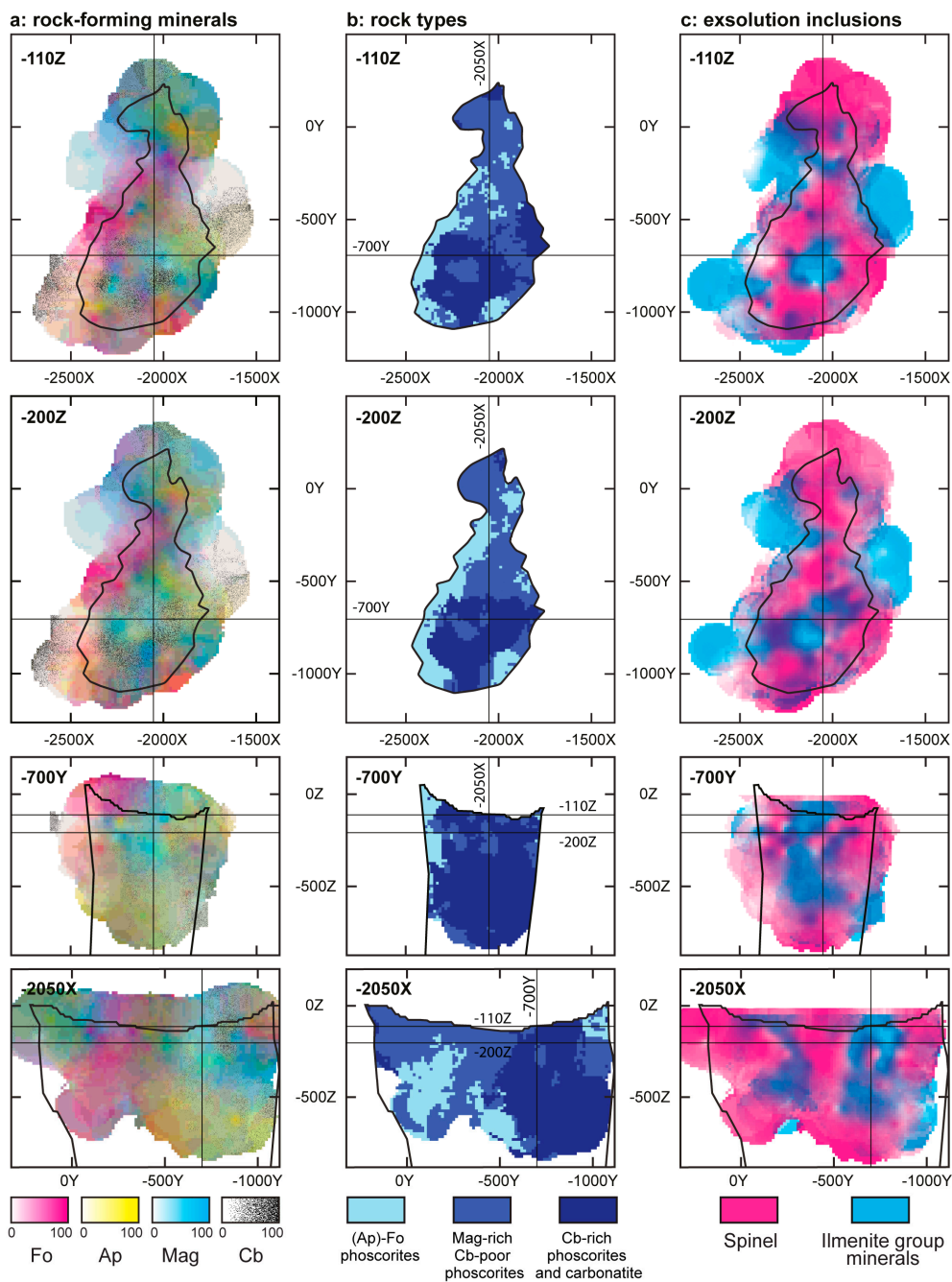


**Figure 2.** Distribution of magnetite (cyan), forsterite (magenta), apatite (yellow), and calcite (black spots) within the Kovdor phoscorite-carbonatite pipe (a), corresponding rock-types (b) and occurrence of magnetite with exsolution inclusions of spinel and minerals of the ilmenite group (c). Cartesian coordinates are in meters, with ordinate axis oriented northwards. Black contour is the boundary of the phoscorite-carbonatite pipe. Ap, apatite; Fo, forsterite; Mag, magnetite; Cb, carbonates (mostly calcite and dolomite).

**Table 2.** Petrography of phoscorite, carbonatites and host silicate rocks of the Kovdor complex.

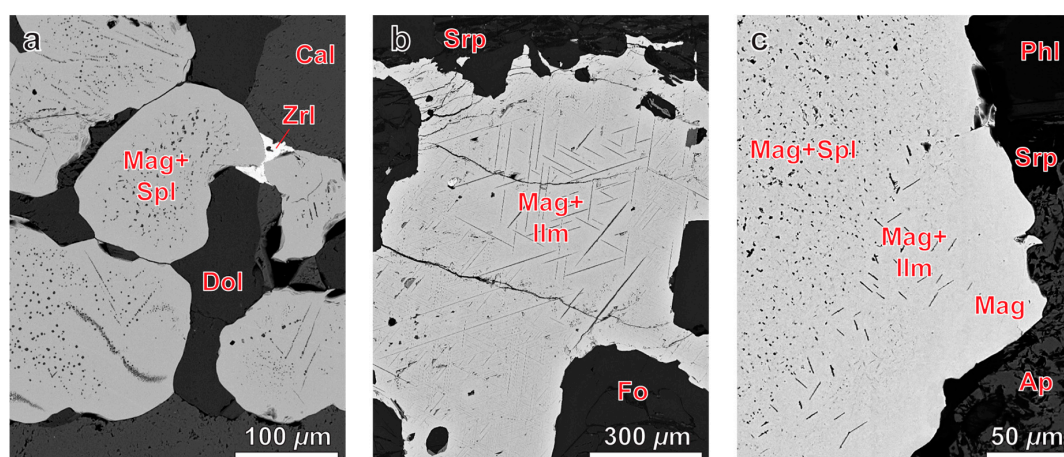
Rock	Description	Modal %	Minor Rock-Forming Minerals	Characteristic Accessories	Magnetite
Foidolite	Dark grey, medium- to fine-grained rock with massive or banded structure formed by alternating leucocratic nepheline-rich and melanocratic clinopyroxene- (Di–Aeg) and/or melilite-rich layers	Nph 10–50 Cpx 50–90 Phl 1–8 Me 0–10	Cancrinite, magnetite, microcline, monticellite, natrolite, sodalite, titanite	Albite, ancylite-(Ce), andradite, baddeleyite, banalcite, barite, bornite, calcite, chalcopyrite, fluorapatite, galena, gonnardite, ilmenite, nordstrandite, nyerereite, pentlandite, perovskite, pyrite, pyrrhotite, pyrochlore, shortite, sphalerite, spinel, strontianite, thorianite	Irregularly shaped grains and skeletal crystals (0.2 ± 0.3 mm)
Diopside and phlogopitite	Dark-green, medium- to coarse-grained massive rock composed mostly of short-prismatic diopside crystals, corroded by phlogopite lamellae. In phlogopitite, there are mica segregations (up to 1 cm in diameter) with diopside relics and newly-formed inclusions of hydroxylapatite and magnetite	Di 10–95 Phl 3–95 Fo 0–30 Nph 0–15	Calcite, cancrinite, clinochlore, dolomite, edenite, gonnardite, hydroxylapatite, magnesioarfvedsonite, magnesiohastingsite, magnetite, natrolite, pargasite, pyrrhotite, richterite, serpentine, sodalite, vermiculite	Aegirine, albite, ancylite-(Ce), baddeleyite, barite, barytocalcite, calzirtite, cerussite, chalcopyrite, chamosite, chromite, cobaltpentlandite, freudenbergite, galena, grinalite, ilmenite, lueshite, mesolite, microcline, pentlandite, perovskite, pyrite, pyrochlore, pyrophanite, rutile, shortite, sphalerite, spinel, titanite, zircon, zirconolite	Irregularly shaped grains (1.0 ± 0.9 mm) in interstices of rock-forming silicates, and larger metacrysts (up to 5 mm) with poikilitic inclusions of surrounding minerals
(Ap)-Fo phoscorite	Greenish-gray fine-grained, massive, indistinctly banded or spotted rock consisting of rounded equant to short-prismatic grains of forsterite. Interstices between forsterite grains are filled with hydroxylapatite (±magnetite) that also forms monomineralic segregations and bands. Phlogopite replaces the forsterite.	Fo 10–90 Ap 0–80 Mag 0–8 Cal 0–5 Phl 1–10	Calcite, diopside, dolomite, magnetite	Baddeleyite, brucite, chalcopyrite, cobaltpentlandite, geikielite, ilmenite, monazite-(Ce), pentlandite, pyrite, pyrochlore, pyrophanite, pyrrhotite, serpentine, sphalerite, spinel, strontianite, valleriite, zirconolite	Anhedral grains (0.2 ± 0.1 mm) in interstices of forsterite; rounded grains (0.3 ± 0.1 mm) and larger metacrysts (up to 8 mm) in apatite-rich parts of the rock
Low-Cb Mag-rich phoscorite	Light greenish-grey to black, massive, spotted, spotty-banded rock consisting mainly of forsterite (altered grains, partially replaced by serpentine, clinochlore, phlogopite and valleriite) and hydroxylapatite (lens-like segregations of rounded or irregularly shaped grains) cemented by magnetite	Fo 0–70 Ap 0–70 Mag 10–95 Cal 0–8	Calcite, chalcopyrite, dolomite, phlogopite, pyrrhotite, valleriite	Ancylite-(Ce), baddeleyite, bakhchisaraitsevite, barite, betafite, bobierite, cobaltpentlandite, galena, geikielite, ilmenite, lueshite, magnesite, perovskite, pentlandite, pyrite, pyrochlore, pyrophanite, quintinite, sphalerite, spinel, thorianite, zirconolite	Irregularly shaped grains (3 ± 2 mm) and larger metacrysts (up to 2 cm) with inclusions of surrounding apatite-forsterite aggregates and separate grains of these minerals
Cb-rich phoscorite and phoscorite-related carbonatite	Spotted black-and-white rocks composed of forsterite (replaced by serpentine, dolomite, phlogopite, clinohumite and clinochlore), hydroxylapatite (anhedral grains between forsterite crystals, inclusions in calcite and monomineralic segregations), magnetite (irregularly shaped metacrysts in apatite-rich parts and well-shaped octahedral crystals in calcite-rich parts) and calcite (monomineralic veinlets and nests between grains of forsterite, hydroxylapatite and magnetite).	Fo 0–70 Ap 0–60 Mag 8–80 Cal 10–82 Dol 1–10 Phl 0–15 Po 0–30 Cp 0–10	Clinochlore, clinohumite, richterite, tetraferriphlogopite, valleriite	Ancylite-(Ce), baddeleyite, bakhchisaraitsevite, barite, baritocalcite, bobierite, bornite, burbankite, chalcocite, cobaltpentlandite, covellite, crandallite, cubanite, djerfisherite, galena, geikielite, ilmenite, juoniite, kovdorskite, mackinawite, magnesite, microlite, norsethite, northupite, nyerereite, perovskite, pyrite, pyrochlore, pyrophanite, quintinite, siderite, sphalerite, spinel, strontianite, thorianite, witherite, zircon, zirconolite	Rounded grains (4 ± 2 mm), larger metacrysts (up to 5 cm) with poikilitic inclusions of forsterite and hydroxylapatite, as well as well-shaped crystals with octahedral {111}, rhombic dodecahedral {110} and tetragonal trioctahedral {311} faces

Table 2. Cont.

Rock	Description	Modal %	Minor Rock-Forming Minerals	Characteristic Accessories	Magnetite
Vein Cal carbonatite	White, light brown or light grey medium- to coarse-grained, massive to banded rock consisting of equant crystals of calcite and dolomite with interstitial hydroxylapatite, magnetite and phlogopite	Fo 0–5 Ap 0–15 Mag 0–10 Cal 70–95 Dol 5–15	Forsterite, magnetite, phlogopite, pyrrhotite	Alstonite, ancylite-(Ce), baddeleyite, barite, calzirtite, chalcocopyrite, cobaltpentlandite, djerfisherite, eitelite, galena, geikielite, ilmenite, microlite, monazite-(Ce), northupite, nyerereite, perovskite, pyrite, serpentine, sphalerite, spinel, strontianite, thorianite, zirconolite	Rounded grains ( $2 \pm 1$ mm) and well-shaped octahedral crystals (up to 3 cm in diameter) with minor rhombic dodecahedral faces
Vein Dol carbonatite	White, pale-pink or light-brown medium- to coarse-grained rock composed mainly of dolomite, with magnetite and pyrrhotite in selvages	Fo 0 Ap 0–6 Mag 0–40 Dol 50–95 Cal 5–10 Po 0–10	Pyrite, richterite, phlogopite, serpentine, tetraferriphlogopite	Anatase, ancylite-(Ce), aragonite, baddeleyite, bakhchisaraitsevite, baricite, barite, barytocalcite, bobierite, burbankite, catapleite, chalcocopyrite, collinsite, hydroxylapatite, ilmenite, juonniite, kovdorskite, labuntsovite-Mg, lueshite, magnesite, norsethite, rimkorolite, serpentine, siderite, sphalerite, spinel, strontianite, zircon, zirconolite	Rounded grains ( $3 \pm 2$ mm) and well-shaped octahedral crystals (up to 4 cm) with minor rhombic dodecahedral faces
Mag-Dol-Srp rock	Dark green to black, fine-grained rock with massive, mottled or brecciated structure. Consists mainly of small grains of dolomite, phlogopite, serpentine (with phlogopite and forsterite relics), and poikilitic magnetite metacrysts of different size and shape	Fo 0–10 Ap 8–25 Mag 20–50 Dol 10–40 Srp 15–30 Phl 5–30	Calcite, pyrrhotite, tetraferriphlogopite	Baddeleyite, baritocalcite, chalcocopyrite, cobaltpentlandite, pentlandite, sphalerite, galena, strontianite, zircon, zirconolite	Irregularly shaped porous metacrysts ( $2 \pm 1$ mm) with numerous inclusions of phlogopite, apatite, calcite, dolomite and fragments of surrounding rock

Mineral abbreviations: Ap, hydroxylapatite; Cal, calcite; Cb, carbonate; Ccp, chalcocopyrite; Cpx, clinopyroxene; Di, diopside; Dol, dolomite; Fo, forsterite; Mag, magnetite; Me, melilite; Nph, nepheline; Phl, phlogopite; Po, pyrrhotite; Srp, serpentine.

In the Kovdor phoscorite-carbonatite pipe, magnetite grains contain almost always (oxy)exsolution inclusions of earlier minerals of the ilmenite group and/or later spinel [40,41,54,55]. In host foidolites, diopsidite and phlogopitite, magnetite grains are usually impregnated with oxy-exsolution inclusions of ilmenite-geikielite (Figures 2 and 3a). Within the phoscorite-carbonatite ore-pipe, forsterite-rich phoscorite of the marginal zone and carbonate-rich phoscorite and carbonatites of the axial zone also contain magnetite with inclusions of ilmenite-geikielite (Figures 2 and 3b), while low-carbonate magnetite-rich phoscorite of intermediate zone predominantly include magnetite with inclusions of spinel. In all phoscorite varieties and carbonatites, especially in magnetite-rich phoscorite of the intermediate zone, there occur grains of magnetite with a spinel-impregnated core initially rimmed by ilmenite-geikielite-impregnated magnetite and then by inclusion-free magnetite (Figures 2 and 3c). In vein calcite and dolomite carbonatites, as well as magnetite-dolomite-phlogopite-serpentine rock, magnetite contains mainly oxy-exsolution lamellae of ilmenite (predominantly) or geikielite.



**Figure 3.** BSE-images of magnetite grains with (oxy)exsolution inclusions of spinel (a) CMAF-phoscorite 985/115.2; ilmenite (b) FM-phoscorite 949/241.6 and both spinel and ilmenite (c) magnetite-dolomite-phlogopite-serpentine rock 961/109.0. Ap, apatite; Cal, calcite; Fo, forsterite; Ilm, ilmenite; Mag, magnetite; Phl, phlogopite; Spl, spinel; Srp, serpentine; Zrl, zirconolite.

As was shown in [16,40], magnesium is the main subordinate component in magnetite of the Kovdor phoscorite-carbonatite complex. There is a minor increase in MgO in magnetite from earlier (apatite)-forsterite phoscorite ( $4 \pm 2$  wt %) to intermediate low-carbonate magnetite-rich phoscorite ( $5 \pm 2$  wt %), and then MgO in magnetite decreases in late carbonate-rich phoscorite and carbonatite ( $4 \pm 2$  wt %). Magnetite with a higher  $Al_2O_3$  content occurs in the intermediate low-carbonate magnetite-rich phoscorite ( $0.7 \pm 0.5$  wt %), while earlier (apatite)-forsterite phoscorite and late carbonate-rich phoscorite and carbonatite contain magnetite with lower content of  $Al_2O_3$  ( $0.5 \pm 0.5$  and  $0.6 \pm 0.9$  wt % correspondingly). The  $TiO_2$  content decreases from earlier (apatite)-forsterite phoscorite ( $2 \pm 1$  wt %) to intermediate low-carbonate magnetite-rich phoscorite ( $1.0 \pm 0.6$  wt %), and then slightly increases in late carbonate-rich phoscorite and carbonatite ( $1.1 \pm 0.9$  wt %). MnO content in magnetite is constant through all the pipe volume ( $0.5 \pm 0.2$  wt %).

It is obvious that magnetite composition determines both the modal and chemical composition of (oxy)exsolution inclusions. This fact enables us to complement the schemas of spatial distribution of the ilmenite-group minerals and spinel (see Figure 2) with similar schemas of their chemical composition and temperature of magnetite (oxy)exsolution. In addition, the shape and grain size of the inclusions will be estimated and correlated with temporal/spatial distribution of (oxy)exsolution temperature and oxygen fugacity.

### 3. Materials and Methods

For this study, we used 540 polished thin sections of phoscorite (mainly), carbonatites and host rocks from 108 exploration holes drilled within the Kovdor phoscorite-carbonatite ore-pipe [16]. The polished thin sections were analyzed using the scanning electron microscope LEO-1450 (Carl Zeiss Microscopy, Oberkochen, Germany) with an energy-dispersive X-ray analytical attachment (EDS) Röntek to obtain back-scattered electron (BSE) images of important regions and pre-analyze all minerals found in the samples under analysis. The Image Tool 3.04 (The University of Texas Health Science Center, San Antonio, TX, USA) was used to generate digital images from the BSE-images, and determine inclusions/magnetite area ratios and inclusions size (equivalent circular diameter of spinel grains, and thickness of ilmenite-geikielite lamellae).

The chemical composition of magnetite–magnesioferrite crystals and (oxy)exsolution inclusions (>10 µm thick/diameter) was determined using the electron probe microanalyzer (EPMA) Cameca MS-46 (Cameca, Gennevilliers, France) operating in wavelength-dispersive mode at 20 kV and 20–30 nA. Grains were analyzed using the beam size of 5 µm and the counting time of about 20 and 10 s on peaks and background respectively. The standards used, and limits of accuracy are given in Table 3. Cation and end-member contents were calculated using the MINAL program of Dmitry D. Dolivo-Dobrovolsky [58]. Equilibrium temperatures and oxygen fugacities of magnetite exsolution were estimated using Fe-Ti two-oxide geothermometers and oxygen-barometers of Andersen and Lindsley [44] and Ghiorso and Evans [49], with corresponding interactive programs ILMAT [59] and MELTS [60]. Statistical analyses were carried out using the STATISTICA 8.0 (StatSoft) and TableCurve 2.0 (The University of Texas Health Science Center, San Antonio, TX, USA) programs. For the statistics, resulting values of the analyses below the limit of accuracy (see Table 3) were considered to be ten times lower than the limit. Geostatistical studies and 3D modeling were conducted with the MICROMINE 16 program. Interpolation was performed with ordinary kriging. The automatic 3D geological mapping (see Figure 2b) was performed by means of chemistry-to-mineral conversion [61].

**Table 3.** Parameters of EPMA analyses.

Element	Limit of Accuracy, wt %	Standards for Wavelength Dispersive X-ray Spectroscopy (WDS) Analyses
Mg	0.1	Pyrope
Al	0.05	Pyrope
Si	0.05	Diopside
Ca	0.03	Diopside
Sc	0.02	Thortveitite
Ti	0.02	Lorenzenite
V	0.1	Metallic vanadium
Cr	0.02	Chromite
Mn	0.01	Synthetic MnCO <sub>3</sub>
Fe	0.01	Hematite
Co	0.01	Metallic cobalt
Ni	0.01	Metallic nickel
Zn	0.01	Synthetic ZnO
Nb	0.05	Metallic niobium
Ta	0.05	Metallic tantalum

### 4. Results

#### 4.1. Spinel

According to the earlier evidence of Rimskaya-Korsakova [41], exsolution spinel forms spherical grains (up to 20 µm in diameter), well-shaped octahedral crystals (up to 200 µm in diameter) as well as six-beam (on [100]) and eight-beam (on [111]) skeletal crystals (up to 300 µm in diameter) structurally

co-oriented with host magnetite crystals. In different sections of host magnetite crystals (Figure 4), these inclusions appear as circles (any sections of magnetite crystals); squares and crosses (on (100) planes); triangles, hexagons and three-beam stars (on (111) planes); rhombs, hexagons, crosses and lamellae (on (110) planes). The content of spinel inclusions in magnetite reaches 27 modal %, and their median content in spinel-containing grains is 9 modal %. Spinel inclusions are mainly concentrated in the cores of magnetite crystals, where their size increases significantly (see Figure 3). Comparatively large crystals of spinel (>20  $\mu\text{m}$  in diameter) are usually rimmed by an inclusion-free magnetite aureole of twice the diameter (see Figure 4).

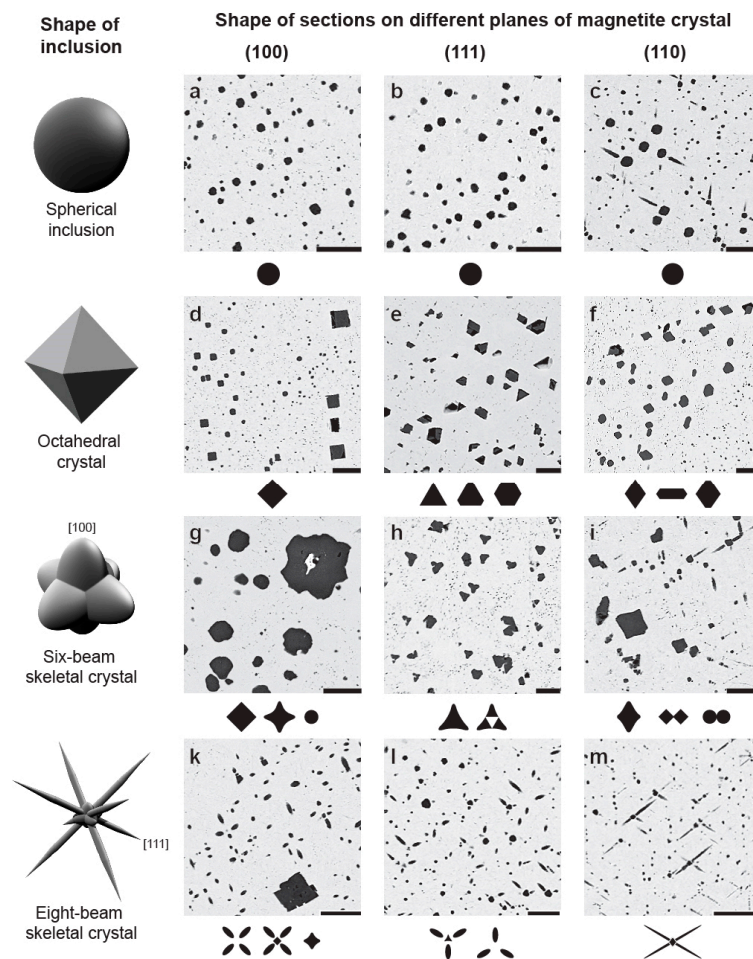
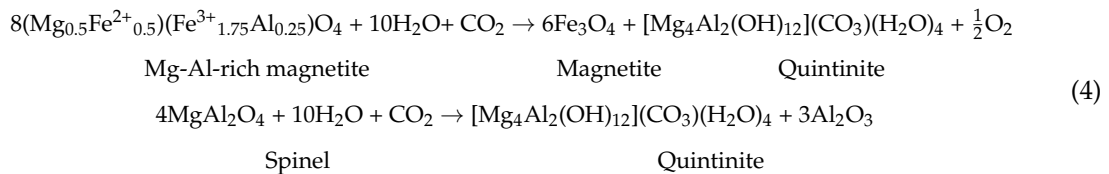


**Figure 4.** Morphology of exsolution inclusions of spinel in magnetite (BSE-images of polished thin sections of phoscorite and their interpretation after [41]). (a) MAF-phoscorite 971/481.8; (b) MAF-phoscorite 933/145.1; (c) CMAF-phoscorite 973-141.4; (d) phoscorite-related carbonatite 1006/169.0; (e) MAF-phoscorite 941/9.6; (f) CMF-phoscorite 957/118.0; (g) CMA-phoscorite 956/138.9; (h) CMA-phoscorite 912/178.6; (i) MAF-phoscorite 951/85.7; (k) CMAF-phoscorite 1010/85.4; (l) MF-phoscorite 917/318.5; (m) MAF-phoscorite 933/214.3. The scale bar is 20  $\mu\text{m}$ .

Spinel crystals commonly contain prismatic inclusions of baddeleyite as a co-product of magnetite exsolution, and sometimes most of the spinel crystals carry such inclusions. During the last stages of magnetite exsolution in the carbonate-rich rocks, quintinite-2H formed after, or instead of, spinel [62]:



The distribution of the grain size of spinel inclusions in magnetite can be of two types (Figure 5): (1) negative-exponential distributions (about 30% of investigated specimens), when cumulative frequencies are concave down in log-log space and linear in semilog space; and (2) power-law distributions (about 70% of investigated specimens), when cumulative frequencies are linear in log-log space and concave up in semilog space. Within different magnetite grains in the same specimen, the size of inclusions is distributed according to the same law. The simplified explanation of the difference between these types of distributions of spinel grain size is that the negative-exponential distribution reflects size-independent crystal growth, and the power-law distribution results from a positive-feedback process in which the time-averaged crystal growth rate is proportional to the crystal size [63–65]. Size-independent growth of spinel occurs in about 30% of low-carbonate magnetite-rich phosphorite of the intermediate zone, and carbonate-rich phoscorite and phoscorite-related carbonatite of the ore-pipe axial zone; however, the size-dependent growth of spinel grains is dominant everywhere (Figure 6).

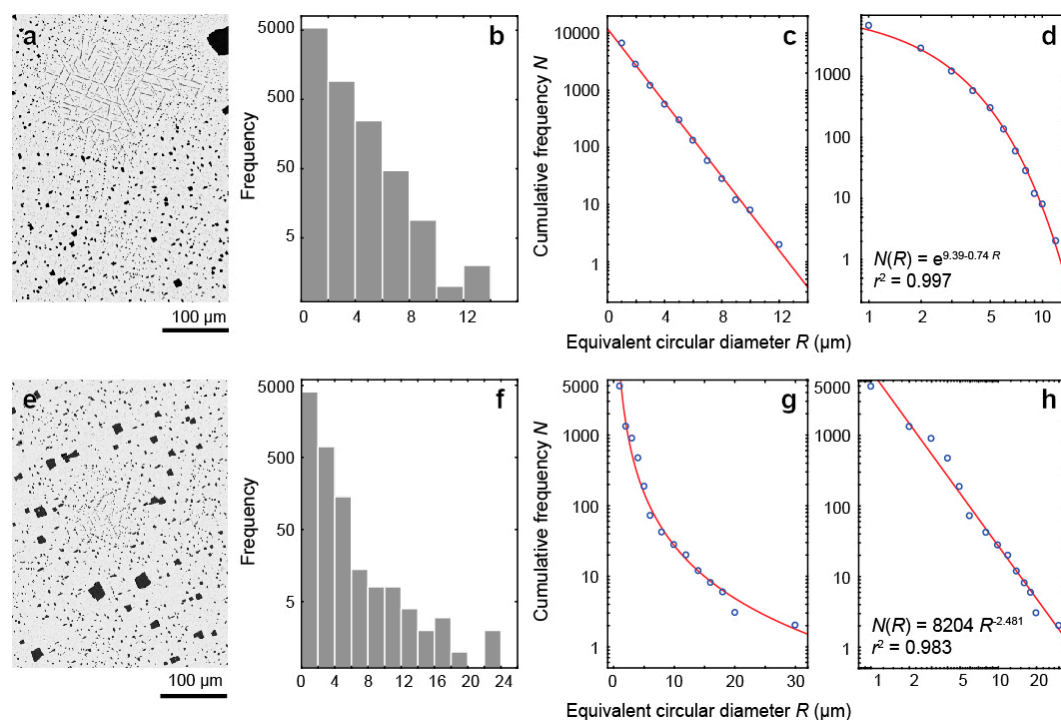


**Figure 5.** BSE-images (a,e), typical histograms (b,f) and cumulative frequency diagrams (c,d,g,h) for equivalent circular diameter of spinel grains when their growth rate is independent of grain size ((a–d) MAF-phoscorite 996/208.2) and proportional to grain size ((e–h) CMAF-phoscorite 1010/85.4).

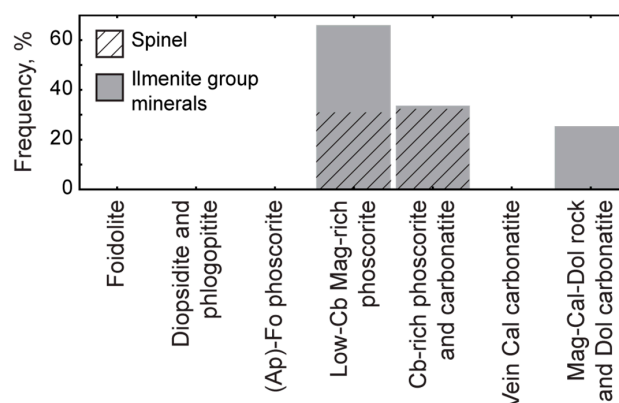


**Figure 6.** Occurrence of samples with negative-exponential distribution of grain size (size-independent growth) of spinel and ilmenite group minerals. The rest samples are characterized by power-law distribution of inclusion size (size-dependent growth).

The typical size of spinel inclusions  $D_{\text{char}}$  (average equivalent circular diameter of a grain fraction with the largest summary area [40,66]) usually lies within the interval of 1–4  $\mu\text{m}$ ; however, in size-dependent sets, an additional maximum appears at 12–50  $\mu\text{m}$  (Figure 7). For this reason,  $D_{\text{char}}$  has a bimodal distribution with maxima at these intervals.

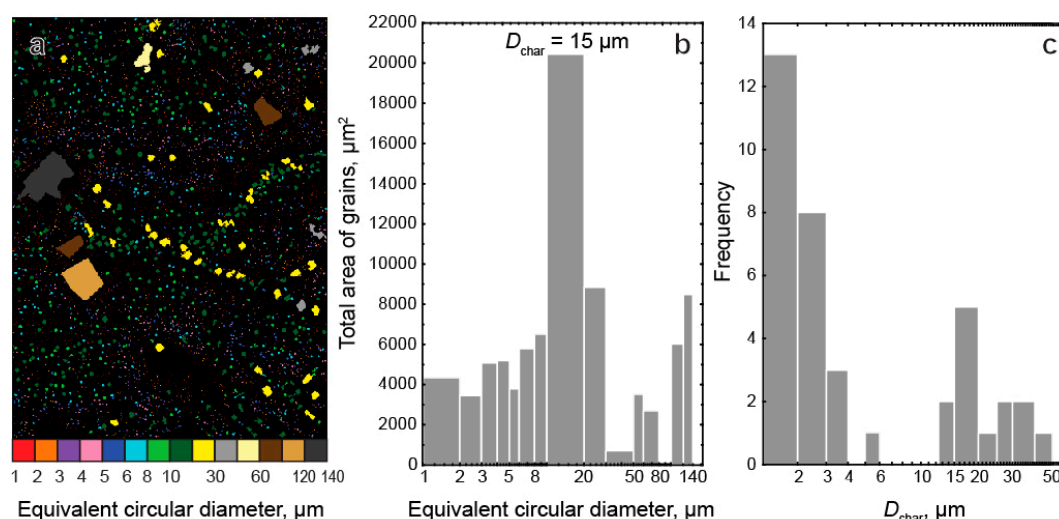


**Figure 7.** Spinel inclusions of different size in a magnetite grain of magnetite-dolomite-serpentine rock 991/61.8 (a); distribution of their equivalent circular diameter (b) and distribution of a typical equivalent circular diameter  $D_{\text{char}}$  (average equivalent circular diameter of a grain fraction with the largest summary area) in the analyzed samples of phosphorite and carbonatites (c).

Typical chemical compositions of magnetite-spinel pairs, selected on the basis of median contents of Mg in spinel, is presented in Table 4. Spinel contains insignificant amounts of chemical impurities, and, on average, its composition corresponds to the formula  $(\text{Mg}_{0.88}\text{Fe}^{2+}_{0.10}\text{Zn}_{0.02})_{\Sigma 1.00}(\text{Al}_{1.86}\text{Fe}^{3+}_{0.13}\text{Ti}_{0.01})_{\Sigma 2.00}\text{O}_4$  [40]. The main compositional impurity is iron that replaces both Mg and Al during exsolution of Mg-Al-rich magnetite (Figure 8a). This process is also accompanied by the differentiation of Mn that remains in the magnetite structure (Figure 8b), and Zn that goes from magnetite into spinel. As a result, in the forsterite-rich phosphorite of marginal zone of the ore-pipe, the exsolved spinel is comparatively enriched both in  $\text{Fe}^{2+}$  and  $\text{Fe}^{3+}$ , and contains higher amounts of  $\text{Fe}^{3+}$  in the carbonate-rich phosphorite and carbonatite of the axial zone (compare Figures 2 and 9).

**Table 4.** Chemical compositions of magnetite-spinel pairs with median content of Al in magnetite.

Rock Group	Foidolite		Diopside and Phlogopitite		(Ap)-Fo Phoscorite		Low-Cb Mag-rich Phoscorite		Cb-rich Phoscorite and PhoscoriteRelated Carbonatite		Vein Cal Carbonatite		Vein Dol Carbonatite and Mag-Dol-Srp Rock	
Sample Rock	971/609.8 Ijolite		900/592.3 Diopside		946/540.4 AF-phoscorite		917/32.8 MF-phoscorite		1007/33.0 Cal carbonatite		989/92.2 Cal carbonatite		977/129.5 Mag-Dol-Srp rock	
Mineral	Mag	Spl	Mag	Spl	Mag	Spl	Mag	Spl	Mag	Spl	Mag	Spl	Mag	Spl
MgO	5.74	24.53	6.57	24.93	4.23	23.50	5.65	25.15	6.43	25.17	8.14	25.55	7.12	25.35
Al <sub>2</sub> O <sub>3</sub>	0.80	66.86	0.69	64.94	0.67	64.72	0.71	66.21	0.74	64.49	0.88	64.46	0.69	67.02
CaO	-	-	-	-	-	-	-	-	0.03	-	-	-	-	-
TiO <sub>2</sub>	0.75	-	1.04	-	1.20	-	0.77	-	0.91	-	0.69	0.09	0.59	-
V <sub>2</sub> O <sub>3</sub>	0.04	-	0.07	-	0.17	-	0.08	-	0.06	-	0.05	-	0.03	-
MnO	0.53	0.10	0.52	0.09	0.50	0.13	0.55	0.25	0.56	0.10	0.53	0.17	0.39	0.08
FeO	84.54	7.05	85.07	7.76	86.79	7.40	85.68	6.94	84.77	8.23	85.47	7.57	86.32	6.00
ZnO	-	1.56	-	0.96	-	1.55	-	1.31	-	1.26	-	1.13	-	1.07
<b>Total</b>	<b>92.40</b>	<b>100.10</b>	<b>93.96</b>	<b>98.68</b>	<b>93.56</b>	<b>97.30</b>	<b>93.44</b>	<b>99.86</b>	<b>93.50</b>	<b>99.25</b>	<b>95.76</b>	<b>98.97</b>	<b>95.14</b>	<b>99.52</b>
<b>Cation Content on the Basis of 4 O and 3 Me a.p.f.u. (atoms per formula unit)</b>														
Fe <sup>2+</sup>	0.69	0.07	0.66	0.06	0.78	0.08	0.70	0.05	0.66	0.05	0.58	0.04	0.63	0.05
Mg	0.32	0.90	0.35	0.92	0.23	0.89	0.31	0.92	0.35	0.93	0.42	0.94	0.38	0.92
Mn	0.02	-	0.02	-	0.02	-	0.02	0.01	0.02	-	0.02	-	0.01	-
Zn	-	0.03	-	0.02	-	0.03	-	0.02	-	0.02	-	0.02	-	0.02
Fe <sup>3+</sup>	1.92	0.07	1.91	0.10	1.91	0.07	1.92	0.09	1.92	0.12	1.92	0.12	1.93	0.07
Al	0.03	1.93	0.03	1.90	0.03	1.93	0.03	1.91	0.03	1.88	0.04	1.88	0.03	1.94
Ti	0.02	-	0.03	-	0.03	-	0.02	-	0.02	-	0.02	-	0.02	-
<b>Total</b>	<b>3.00</b>	<b>3.00</b>	<b>3.00</b>	<b>3.00</b>	<b>3.00</b>	<b>3.00</b>	<b>3.00</b>	<b>3.00</b>	<b>3.00</b>	<b>3.00</b>	<b>3.00</b>	<b>3.00</b>	<b>3.00</b>	<b>3.00</b>
<b>End Members, Mole %</b>														
Mag	64.78	0.27	61.20	0.31	72.09	0.31	65.59	0.24	61.64	0.30	54.62	0.22	59.82	0.19
Mfr	29.75	3.23	32.89	4.78	21.40	3.33	29.03	4.19	32.58	5.80	40.18	5.74	35.98	3.21
Jcb	1.64	0.20	1.57	0.20	1.53	0.28	1.66	0.52	1.69	0.22	1.54	0.35	1.15	0.17
Hc	1.18	7.39	0.94	5.70	1.11	8.25	1.04	5.18	1.02	4.60	1.03	3.51	0.89	5.40
Spl	0.54	88.91	0.51	89.01	0.33	87.82	0.46	89.87	0.54	89.08	0.76	90.00	0.54	91.03
Usp	1.40	-	1.81	-	2.54	-	1.45	-	1.60	-	1.04	0.01	0.98	-
Qnd	0.64	-	0.97	-	0.75	-	0.64	-	0.85	-	0.76	0.17	0.59	-
Cul	0.04	-	0.07	-	0.19	-	0.08	-	0.05	-	0.04	-	0.03	-
Mcul	0.02	-	0.04	-	0.06	-	0.04	-	0.03	-	0.03	-	0.02	-
<b>Total</b>	<b>99.99</b>	<b>100.00</b>	<b>100.00</b>	<b>100.00</b>	<b>100.00</b>	<b>99.99</b>	<b>99.99</b>	<b>100.00</b>	<b>100.00</b>	<b>100.00</b>	<b>100.00</b>	<b>100.00</b>	<b>100.00</b>	<b>100.00</b>

Dash means content below detection level. End members (see Table 1): Cul, coulsonite; Hc, hercynite; Jcb, jacobsonite; Mag, magnetite; Mcul, magnesiocoulsonite; Mfr, magnesioferrite; Qnd, qandilite; Spl, spinel; Usp, ulvöspinel. Other mineral abbreviations: Ap, hydroxylapatite; Cal, calcite; Cb, carbonate; Dol, dolomite; Fo, forsterite; Mag, magnetite; Srp, serpentine.

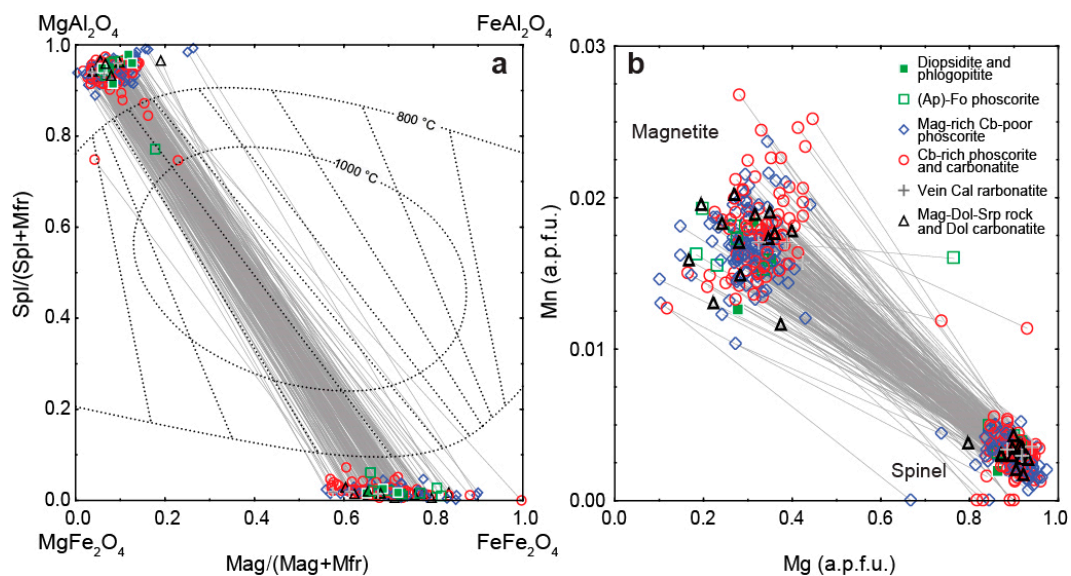


**Figure 8.** Compositions of coexisting spinel-magnetite pairs (joined by grey lines) represented by the combined plane of  $MgFe_2O_4$ - $FeFe_2O_4$  series and  $MgAl_2O_4$ - $FeAl_2O_4$  series (a) (mole %), and corresponding Mg-Mn relation (b). Calculated miscibility gap and tie lines at 800 °C and 1000 °C, 4 kbar (dotted line) are plotted using Lehmann-Roux’s model [45].

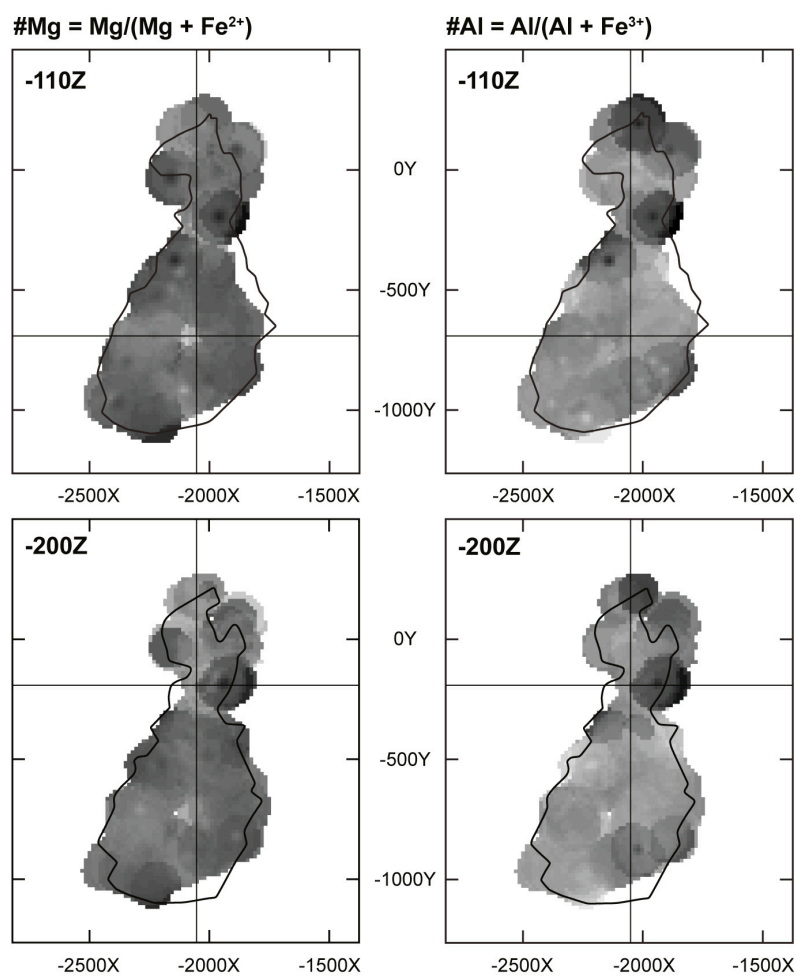


**Figure 9.** Cont.

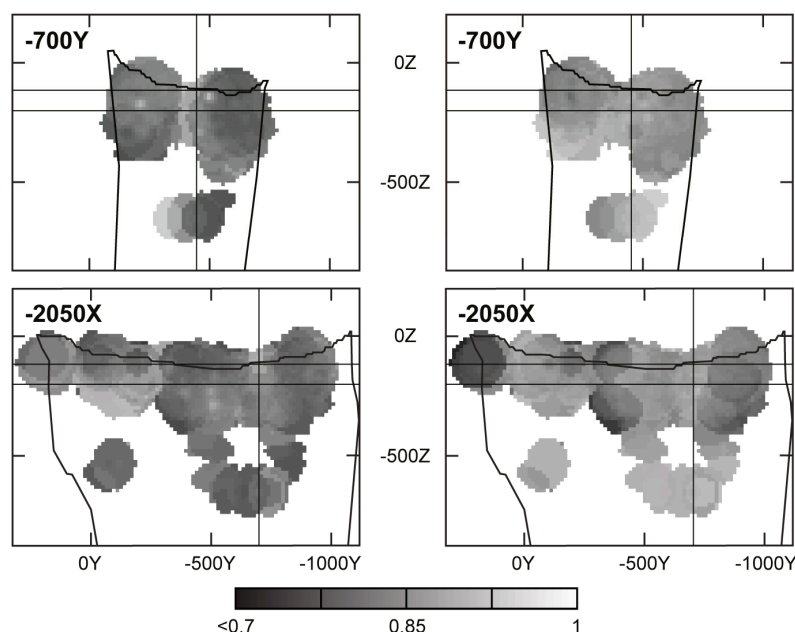


**Figure 9.** Distribution of #Mg and #Al in exsolution spinel within a phoscorite-carbonatite pipe (black contour). See Figure 2 for the comparison.

The diagram in Figure 8a shows compositions of spinel-magnetite pairs in relation to miscibility gaps and equilibrium tie lines in the system of spinels—( $\text{Fe}^{2+}$ , Mg) $\text{Cl}_2$  aqueous solution at 800 °C and 4 kbars [45]. Solid tie lines, connecting compositions of coexisting magnetite and spinel, are nearly parallel to dotted tie lines calculated with the Lehmann-Roux model [45]. The orientation of the tie lines in this model is almost independent of temperature; but pairs of low-temperature origin have much lower mutual solubility. This means that exsolution of Mg-Al-rich magnetite mostly took place at temperatures much lower than 800 °C, and only a few specimens of magnetite-bearing carbonatite showed temperatures of magnetite exsolution between 800 °C and 1000 °C.

#### 4.2. Ilmenite Group Minerals

Ilmenite, geikielite and pyrophanite (generic term ilmenite) usually occur as thin (up to 50  $\mu\text{m}$  thick) lamellae oriented along the {100} and {111} planes of host magnetite [40,42,54,67], and form characteristic trellises on all other planes (see Figure 3b,c). Lamellae oriented along the {111} planes of magnetite are predominant and originate from reaction (2), while their orientation along the {100} planes of magnetite occurs much rarer as a probable result of consecutive reactions (1) and (3) [39,68]. The cores of magnetite crystals contain comparatively thick ilmenite lamellae, while outer zones are often free of inclusions or include the thinnest lamellae of “ilmenite”. The content of “ilmenite” inclusions in magnetite reaches 26 vol %, and their median content in “ilmenite”-containing grains of magnetite is 10 vol %. Sometimes, ilmenite lamellae contain co-oriented inclusions of baddeleyite, and coexist with quintinite in magnetite crystals with spinel-impregnated cores and ilmenite-quintinite bearing marginal zones of titanomagnetite grains.

The distribution of ilmenite lamellae thickness is similar to the distribution of spinel grain diameter (Figure 10): power-law distributions are predominant and negative-exponential distributions occur much more rarely (correspondingly, about 80% and 20% of investigated samples). Just as with spinel, size-independent growth of ilmenite lamellae prevails, and size-dependent growth occurs in magnetite-rich phoscorite and phoscorite-related carbonatite of the ore-pipe intermediate and axial zones, as well as in the latest magnetite–dolomite–(phlogopite)–serpentine rock and vein dolomite carbonatite (see Figure 6). Comparatively large ilmenite lamellae are always rimmed by an aureole of inclusion-free magnetite (see Figure 10).

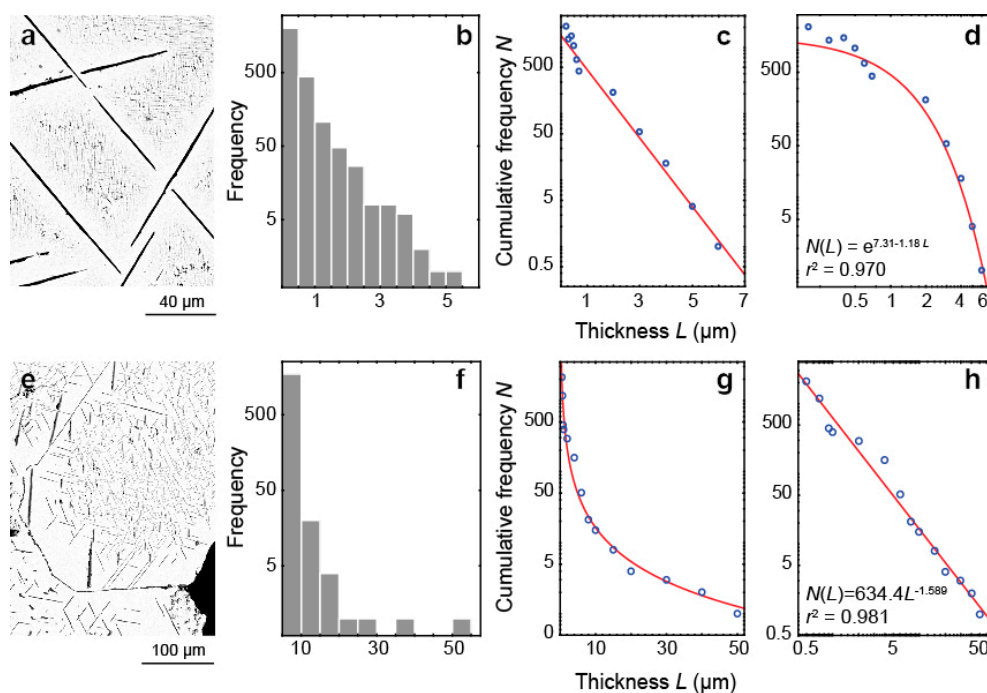


**Figure 10.** BSE-images (a,e), characteristic histograms (b,f) and cumulative frequency diagrams (c,d,g,h) for thickness of ilmenite lamellae for growth rate independent of lamella size ((a–d) MAF-phoscorite 986/147.5) and proportional to lamella size ((e–h) magnetite-dolomite-phlogopite-serpentine rock 976/191.7).

The representative compositions of ilmenite-magnetite pairs from different rocks of the Kovdor massif are shown in Table 5 in accordance with the median content of Ti in ilmenite. On the ternary diagram (Fe, Mg, Mn)O–(Fe, Al)<sub>2</sub>O<sub>3</sub>–TiO<sub>2</sub> (Figure 11a), compositions of co-existing magnetite and oxy-exsolution ilmenite are located along the magnetite–ulvöspinel (titanomagnetite) and hematite–ilmenite (titanohematite) lines, correspondingly. As for divalent cation relations, the ilmenite compositions range widely from ilmenite-poor to geikielite- and pyrophanite-poor, and correspond to average formula of Mg-rich ilmenite: (Fe<sup>2+</sup><sub>0.50</sub>Mg<sub>0.36</sub>Mn<sub>0.13</sub>)<sub>Σ0.99</sub>(Ti<sub>0.96</sub>Fe<sup>3+</sup><sub>0.05</sub>Nb<sub>0.01</sub>)<sub>Σ1.02</sub>O<sub>3</sub> [40]. Fractionation of Mg and Mn between coexisting titanomagnetite and ilmenite (Figure 11b) has resulted in significant losses of Mg in host magnetite in comparison with fresh volcanic rocks [47] due to spinel exsolution following ilmenite oxy-exsolution [39,40].

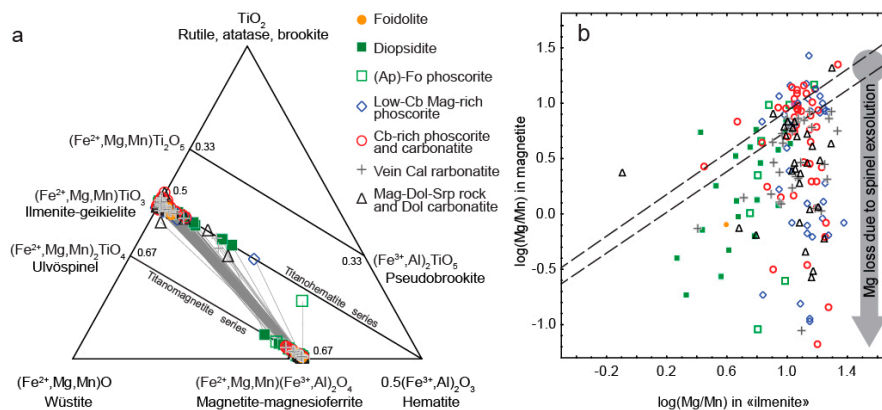
As a result, the spatial distribution of ilmenite composition reflects the total zonation of the Kovdor phoscorite–carbonatite pipe (compare Figures 2 and 12). In particular, higher content of Fe<sup>2+</sup> characterizes oxy-exsolution ilmenite from low-carbonate magnetite-rich phoscorite of the ore-pipe intermediate zone, and from neighboring silicate rocks. Conversely, oxy-exsolution ilmenite with higher content of Mg (up to pure geikielite) is spread over the forsterite-rich marginal zone and carbonate-rich axial zone of the ore-pipe. Manganese-rich oxy-exsolution ilmenite (up to pyrophanite) occurs in marginal forsterite-rich phoscorite, and ilmenite with higher content of Fe<sup>3+</sup> (up to Ti-rich hematite) is spread over (apatite)-forsterite phoscorite of the ore-pipe marginal zone, carbonate-rich phoscorite and carbonatite of the axial zone, and neighboring diopsidite.



Table 5. Cont.

Rock Group	Foidolite	Diopside and Phlogopite		(Ap)-Fo Phoscorite	Low-Cb Mag-Rich Phoscorite		Cb-Rich Phoscorite and Phoscorite-Related Carbonatite		Vein Cal Carbonatite	Vein Dol Carbonatite and Mag-Dol-Srp Rock			
End Members, Mole %													
Mag	96.11		93.70	82.47		86.23		91.98	92.20		87.58		
Mfr	1.17		1.97	10.45		9.88		4.45	4.94		8.63		
Jcb	0.30		0.61	2.28		0.81		0.48	0.39		0.92		
Hc	-		0.34	0.71		-		-	-		-		
Spl	-		0.01	0.09		-		-	-		-		
Usp	0.90		2.38	3.33		2.49		2.63	2.17		2.32		
Qnd	0.01		0.05	0.42		0.28		0.13	0.12		0.23		
Cul	0.56		0.10	0.22		0.27		0.31	0.17		0.28		
Mcul	0.01		-	0.03		0.03		0.02	0.01		0.03		
Ilm		82.00		81.32		53.56		54.48		56.19		53.43	
Ppn		8.13		9.38		13.88		6.13		5.47		7.94	
Gkl		6.50		8.02		30.92		38.35		36.83		37.38	
Hem		3.18		0.99		1.63		0.48		1.00		1.11	
<b>Total</b>	<b>99.06</b>	<b>99.81</b>	<b>99.16</b>	<b>99.71</b>	<b>100.00</b>	<b>99.99</b>	<b>99.99</b>	<b>99.44</b>	<b>100.00</b>	<b>100.00</b>	<b>100.00</b>	<b>99.99</b>	<b>99.86</b>
Temperature (°C) and Oxygen Fugacity													
$T_1$	504		452	504		455		455		651		470	
$T_2$	287		265	289		232		240		411		250	
$\Delta\text{NNO}_1$	+0.15		-4.09	-2.73		-4.47		-4.18		+2.55		-3.29	
$\Delta\text{NNO}_2$	+0.66		-2.80	-3.85		-5.15		-4.66		+0.96		-4.13	

Dash means a content below detection level.  $T_1$  and  $\Delta\text{NNO}_1$  are calculated using the model of Andersen and Lindsley [44],  $T_2$  and  $\Delta\text{NNO}_2$  of Ghiorso and Evans [49]. End members: Cul, coulsonite; Gkl, geikielite; Hc, hercynite; Hem, hematite; Ilm, ilmenite; Jcb, jacobsite; Mag, magnetite; Mcul, magnesiocoulsonite; Mfr, magnesioferrite; Ppn, pyrophanite; Qnd, qandilite; Spl, spinel; Usp, ulvöspinel. Other mineral abbreviations: Ap, hydroxylapatite; Cal, calcite; Cb, carbonate; Dol, dolomite; Fo, forsterite; Mag, magnetite; Srp, serpentine.



**Figure 11.** Composition of magnetite-ilmenite pairs (joined by gray lines) plotted in  $\text{TiO}_2$ – $(\text{Fe}, \text{Mg}, \text{Mn})\text{O}$ – $0.5(\text{Fe}, \text{Al})_2\text{O}_3$  ternary diagram ((a), by atomic proportions), and Mn–Mg exchange test of Bacon and Hirschmann [47] (b). Dashed lines limit the field of pairs in Mn–Mg exchange equilibrium.

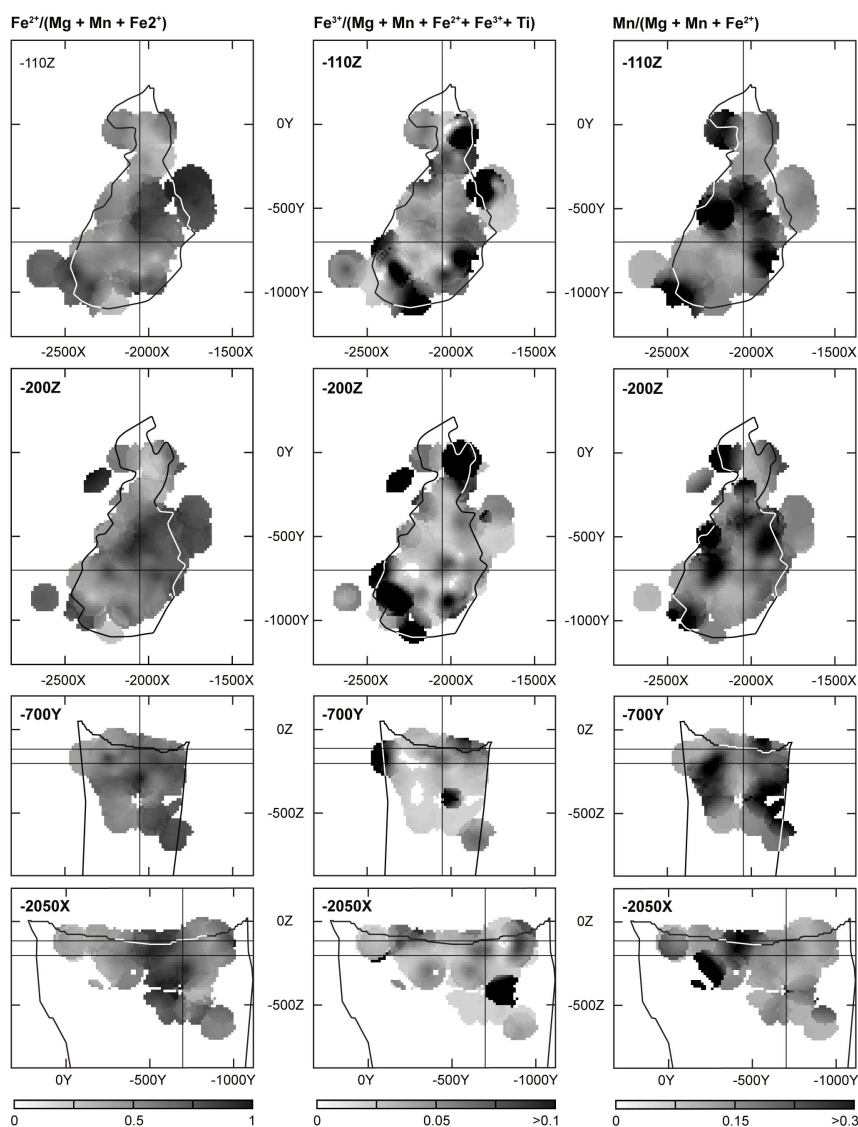


**Figure 12.** Distribution of composition of oxy-exsolution ilmenite within the phoscorite-carbonatite pipe (black/white contour). See Figure 2 for comparison.

Temperatures of titanomagnetite oxy-exsolution,  $T_1$ , and oxygen fugacities,  $\log f_{O_2}$ , for 371 ilmenite-magnetite pairs (177 samples) were determined first using the  $Fe^{2+}Ti-Fe^{3+}_2$  exchange geothermometer/oxometer of Andersen and Lindsley [44], and the model of Stormer [69] for calculation based on molecular fractions. Obtained values of  $\log f_{O_2}$  and  $T_1$  increase from  $-55$  at  $246$  °C to  $-9$  at  $1043$  °C in accordance with the Ni–NiO oxygen fugacity buffer (Figure 13a). However, as was shown [49], this model often gives a temperature and oxygen fugacity that is too high, especially when the oxidation state is estimated under relatively oxidized conditions.

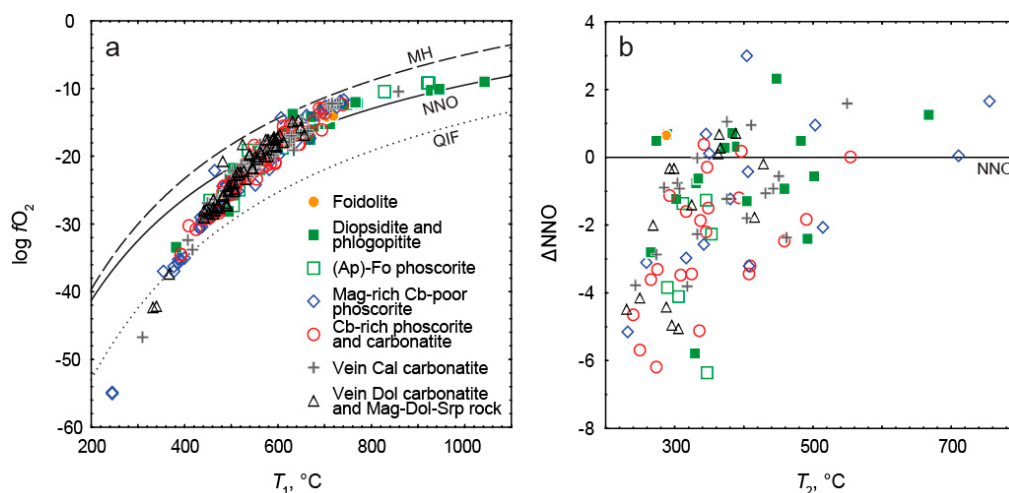


**Figure 13.** Temperature and  $f_{O_2}$  of titanomagnetite oxy-exsolution calculated using the models of Andersen and Lindsley [44] (a), and Ghiorso and Evans [49] (b). Fugacity buffers curves QIF (quartz–iron–fayalite), NNO (nickel–nickel oxide) and MH (magnetite–hematite) are calculated with the Frost’s model [70] at pressure of 200 MPa.

For this reason, more accurate estimation of equilibration temperature,  $T_2$ , and oxygen fugacity deviation from the Ni–NiO oxygen fugacity buffer at 200 MPa,  $\Delta NNO$ , was performed on 94 samples using the  $Fe^{2+}Ti-Fe^{3+}_2$  exchange geothermometer/oxometer of Ghiorso and Evans [49]. This produced estimated values in the range from  $230$  °C to  $756$  °C, and from  $NNO - 6.4$  to  $NNO + 3$  (Figure 13b), with difference between  $T_1$  and  $T_2$  up to  $200$  °C. Unfortunately, almost half of ilmenite-magnetite pairs cannot be estimated with the last model due to unsuitable chemical composition (higher content of Mn, Nb, Sc, etc.), which markedly constrains perspectives of 3D modeling. Nevertheless, there are good regressions between temperatures and oxygen fugacities obtained with both geothermometers/oxometers (Figure 14) that enables to estimate equilibration temperatures and oxygen fugacity values for the rest of the 83 samples using the corresponding equations:

$$\begin{aligned} T_2' &\approx 198.46 + 3.58 \exp(T_1/153.61); \\ \Delta NNO_2' &\approx -1.24 + 0.80 \Delta NNO_1 \end{aligned} \quad (5)$$

Values of  $T_2'$  and  $\Delta NNO'$  obtained this way were added to  $T_2$  and  $\Delta NNO$  values, and then the results were used for statistics and 3D modeling. In the natural sequence of the Kovdor’s rock formation, the oxygen fugacity and temperature of titanomagnetite oxy-exsolution sharply decreased (Figure 15) from host foidolite (on average,  $NNO + 0.7$  at  $517$  °C) to diopsidite and phlogopitite ( $NNO - 0.8$  at  $388$  °C), (apatite)-forsterite phoscorite ( $NNO - 1.4$  at  $347$  °C) and low-carbonate magnetite-rich phoscorite ( $NNO - 1.8$  at  $337$  °C); then again the values increased in carbonate-rich phoscorite, phoscorite-related carbonatite ( $NNO - 0.6$  at  $343$  °C) and vein calcite carbonatite ( $NNO - 0.9$  at  $361$  °C); and decreased to a minimum ( $NNO - 1.9$  at  $316$  °C) in magnetite-dolomite-(phlogopite)-serpentine rock and vein dolomite carbonatite. It is necessary to note that application of geothermometers–geooxometers to magnetite-ilmenite pairs in intrusive rocks does

not correspond the parameters of the rocks formation, but rather reflects the closure of exchange of components between coexisting phases.

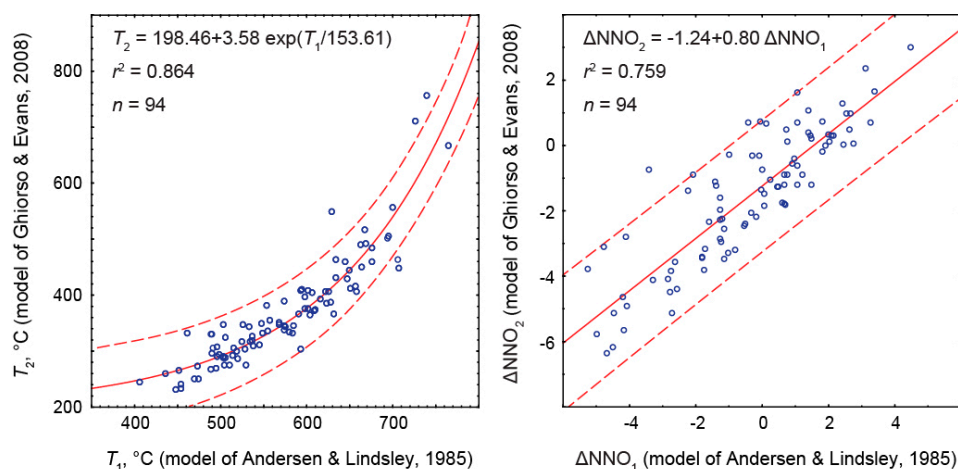


**Figure 14.** Relations between equilibration temperatures and the oxygen fugacity values calculated using magnetite-ilmenite geothermometers of Andersen and Lindsley [44] and Ghiorso and Evans [49]. Dashed lines limit 95% prediction intervals.

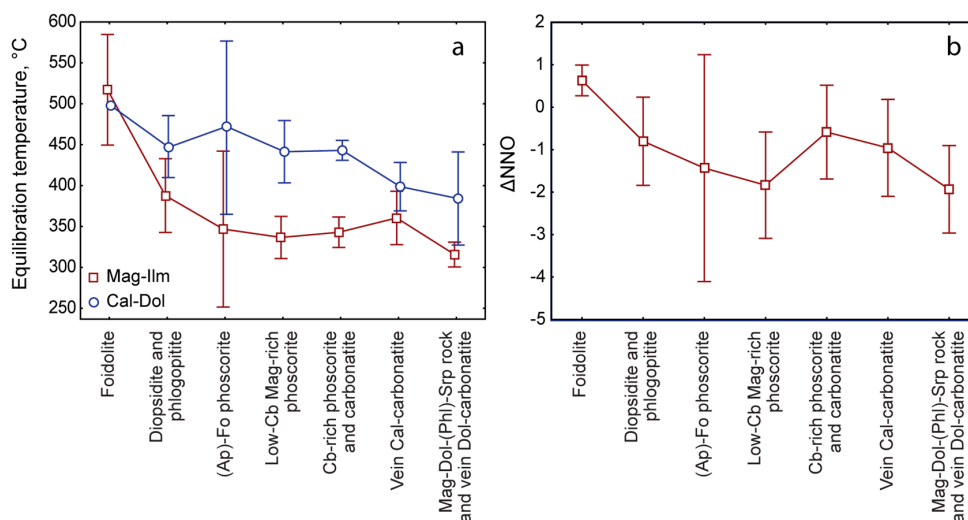


**Figure 15.** Average equilibration temperature (a) and oxygen fugacity (b) of titanomagnetite oxy-exsolution in rocks of the Kovdor massif ( $\pm 95\%$  confidence interval). Results of calcite-dolomite geothermometry with the formulation proposed by Anovitz and Essene [71] are given for comparison.

It was not a surprise when 3D-modeling showed a sharp decrease of both temperature and oxygen fugacity from host silicate rocks and (Ap)-Fo phoscorite of the ore-pipe marginal zone towards magnetite-rich phoscorite of the intermediate zone, with a secondary maximum in carbonate-rich phoscorite and carbonatite of the ore-pipe axial zone (compare Figures 2 and 16).

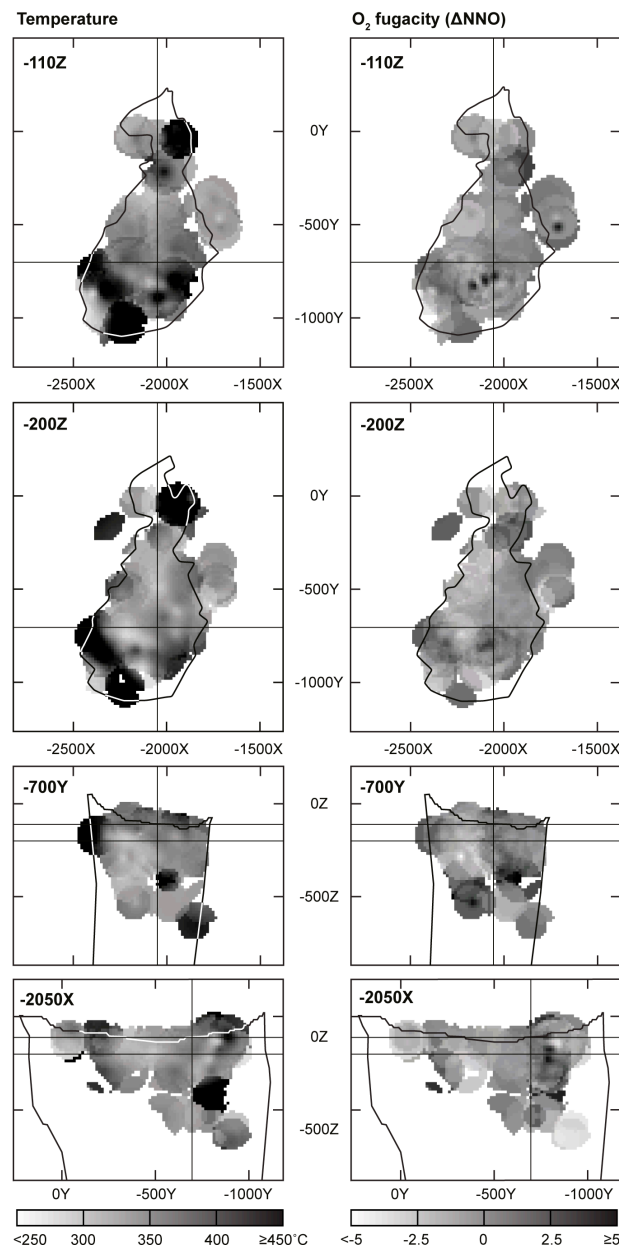


**Figure 16.** Distribution of temperature and oxygen fugacity of titanomagnetite oxy-exsolution within the phoscorite-carbonatite pipe (black/white contour). See Figure 2 for comparison.

## 5. Discussion

As was shown in [16,40,72], the properties and composition of all economic minerals, including magnetite, vary within the phoscorite-carbonatite complex following regular petrographic zonation of the ore-pipe. In particular, Mn-Ti-rich magnetite (with oxy-exsolution inclusions of ilmenite–pyrophanite) of the marginal (apatite)-forsterite phoscorite were replaced by Mg-Al-rich magnetite (with exsolution inclusions of spinel) of the intermediate low-carbonate magnetite-rich phoscorite, and then by Ti-V-rich magnetite (with oxy-exsolution inclusions of geikielite and Mg-rich ilmenite) of carbonate-rich phoscorite and carbonatite of the ore-pipe axial zone. New results allowed us to associate this zonation with thermodynamic conditions of the Kovdor phoscorite-carbonatite complex formation.

Since magnetite (oxy)exsolution is a subsolidus process, estimated temperatures of the magnetite-ilmenite equilibration can differ significantly from the temperatures of

phoscorite-carbonatite melt crystallization. However, the estimated temperature sequence is well complemented by our results from calcite-dolomite geothermometry (using the formulation proposed by Anovitz and Essene [71]) that form an almost linear trend of temperature decrease from foidolite to dolomite carbonatite (see Figure 15). The figure shows that titanomagnetite oxy-exsolution occurs at a temperature that is lower than the temperature for the exsolution of carbonates by 250 °C.

It is generally recognized that intercrystalline diffusion, nucleation and growth of (oxy)exsolution inclusions are temperature-dependent processes. Therefore, the probability of critical nucleus formation is proportional to  $\exp(-\Delta G^*/kT)$ , where  $\Delta G^*$  is a nucleation barrier corresponding to the critical radius of a nucleus, and  $k$  is the Boltzmann constant. The probability increases with temperature decrease because the latter causes an increase in the degree of supersaturation. However, when a stable nucleus is formed, its further growth is significantly constrained by the diffusivities of components [73,74].

The diffusion of cations through the magnetite structure depends on both temperature and oxygen fugacity [75–77]:

$$D^* = D_{[V]}^0 \exp\left(\frac{-H_V}{RT}\right) f_{O_2}^{2/3} + D_{[I]}^0 \exp\left(\frac{-H_I}{RT}\right) f_{O_2}^{-2/3} \quad (6)$$

where  $D^0$  is the temperature independent diffusion coefficient,  $H$  the activation enthalpy for vacancy  $[V]$  and interstitial  $[I]$  regimes,  $f_{O_2}$  the oxygen fugacity in bars,  $R$  the gas constant and  $T$  the temperature in Kelvin. As it follows from this equation, a vacancy mechanism of diffusion prevails under oxidizing conditions ( $\Delta NNO > 0$ ), and decreases with temperature increase; while interstitial diffusion occurs under reducing conditions ( $\Delta NNO < 0$ ) and increases with temperature growth. Besides, the increase of vacancy concentration due to the substitution  $2Fe^{2+} \leftrightarrow V + Ti^{4+}$  decreases the concentration of interstitial cations, and inhibits diffusion of divalent cations by the more “rapid” interstitial mechanism [78].

Estimation of the diffusion coefficients  $D^*$  of Al and Ti in magnetite for the Kovdor phoscorite-carbonatite complex using this equation, with  $D^0$  and  $H$  values given in [77], has shown (Figure 17) that lower cation diffusivities occur in the rocks where size-independent growth of (oxy)exsolution inclusions was found (see Figure 6). Size-independent (constant) crystal growth occurs when equivalent faces on similar crystals grow at the same rate, i.e., increment of the crystal diameter  $dD$  is a constant  $k$  for all crystals, regardless of their size, in each time interval  $dt$ :  $dD/dt = k$  and  $D_{j+1} = D_j + k_j$  [79]. We believe that the constant growth of (oxy)exsolution inclusions in magnetite is caused by slower diffusion rates of cations, which is considered to be the main factor constraining the growth.

Size-dependent (proportional) crystal growth can be mathematically described by the equation  $D_{j+1} = D_j + \varepsilon_j D_j$ , where  $\varepsilon_j$  is a small random number within a narrow range, which differs for each crystal and for each growth cycle [79]. In this case, the increment of each crystal diameter  $dD$  in a certain time interval  $dt$  is proportional to the crystal initial diameter  $D$ :  $dD/dt = kD$ . There are four main explanations of the size-dependent crystal growth [79–82]. Firstly, due to the Gibbs-Thomson effect, equilibrium solubility of fine grains ( $<1 \mu m$ ) decreases with their size growth, consequently, smaller grains will have lower supersaturation, and grow slower. Secondly, concerning the crystals coarser than  $1 \mu m$ , the probability of dislocation occurrence increases with their surface growth, which in turn causes faster growth of such crystals. Thirdly, this can result from surface-controlled growth, and the volume of reactants during each cycle is actually unlimited. Fourthly, it occurs when crystals of the same size grow at different rates.

Although all these mechanisms can cause size-independent growth of (oxy)exsolution inclusions in magnetite, the first of them seems more important. It is necessary to note also that the removal of titanium from the magnetite matrix to a growing ilmenite inclusion causes interstitial diffusion increase, and thus accelerates inclusion growth. Besides, a growing inclusion increases stress in the magnetite matrix, which results in additional dislocations, and activates cation redistribution.

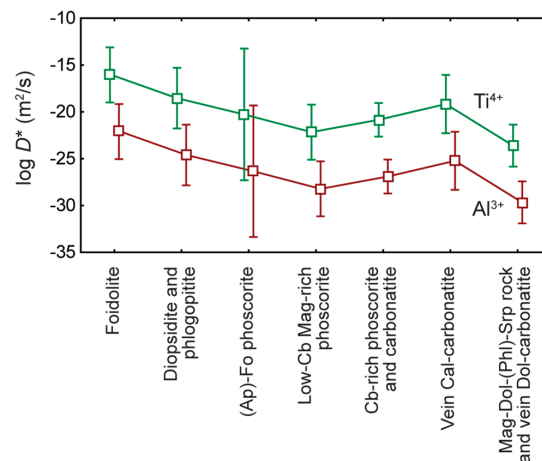


**Figure 17.** Diffusivities of Al and Ti in magnetite during its exsolution in rocks of the Kovdor massif (mean  $\pm$  95% confidence interval).

## 6. Conclusions

Complex (oxy)exsolution of Mn-Mn-Al-Ti-rich magnetite in the Kovdor phoscorite-carbonatite pipe has formed concentric alternating zones of spinel- and ilmenite-impregnated magnetite within the pipe: (apatite)-forsterite phoscorite of the marginal zone and carbonate-rich phoscorite and carbonatite of the axial zone predominantly contain magnetite with exsolution lamellae of ilmenite-geikielite, while low-carbonate magnetite-rich phoscorite of the intermediate zone predominantly includes exsolved magnetite with spinel impregnation. Each of these zones (rock types) has certain features in terms of exsolution processes and products:

- (1) Exsolution spinel forms spherical grains, octahedral crystals, six-beam (along [100]) and eight-beam (along [111]) skeletal crystals co-oriented with host magnetite and having maximal morphological diversity in magnetite-rich phoscorites of the ore-pipe inner part. The ilmenite group minerals occur usually as thin lamellae on the (111) and (100) planes of host magnetite (respectively, due to direct oxy-exsolution of titanomagnetite and with intermediate ulvöspinel). In accordance with the lower diffusivity of Al than Ti in studied magnetites, spinel crystallizes after the ilmenite-group minerals, which is emphasized by the formation of zoned magnetite crystals with spinel-impregnated core, ilmenite-impregnated intermediate zone and inclusion-free marginal zone;
- (2) The kinetics of inclusion nucleation and growth depends mainly on the diffusivity of cations in magnetite: comparatively low diffusivities of Al<sup>3+</sup> and Ti<sup>4+</sup> cations in magnetite- and/or carbonate-rich phoscorite and carbonatite cause size-independent growth of both spinel and ilmenite-group minerals, while higher diffusivities of these cations in surrounding rocks, marginal forsterite-rich phoscorite and vein calcite carbonatite lead to size-dependent growth of corresponding inclusions;
- (3) Three-dimensional mineralogical mapping of the Kovdor phoscorite-carbonatite pipe has shown its concentric (nested) zonation in regard to granulometry, shape, modal and chemical compositions of (oxy)exsolution inclusions in magnetite. In general, this zonation reflects concentric spatial change of host magnetite composition, corresponding in turn to the rock crystallization sequence: surrounding silicate rocks—earlier forsterite-rich phoscorite—intermediate low-carbonate magnetite-rich phoscorite—late carbonate-rich phoscorite and carbonatite;
- (4) Temperature and oxygen fugacity of titanomagnetite exsolution decreases in this sequence from about 500 °C to about 300 °C and from NNO + 1 to NNO – 3, with local positive maximums in

calcite carbonatite. The temperature of magnetite oxy-exsolution in phoscorite and carbonatites is about 250 °C below the temperature of equilibration of coexisting carbonates;

- (5) The intermediate low-carbonate magnetite-rich phoscorite was crystallized under oxidizing conditions resulting in the presence of Fe<sup>3+</sup> instead of Fe<sup>2+</sup> in melt/fluid. Therefore, oxy-exsolution of titanomagnetite finished here at lower temperature, oxygen fugacity and titanium diffusivity than in marginal and axial zones of the ore-pipe.

**Acknowledgments:** The research is supported by the Russian Science Foundation, Grant 16-17-10173. We are grateful to D.V. Dolivo-Dobrovolsky, M.S. Giorso, M.E. Evans and D. Lepage for excellent free software used for mineralogical and thermodynamic calculations. Furthermore, we thank the anonymous reviewers for constructive comments and corrections.

**Author Contributions:** G.Y.I. designed the experiments, performed statistical investigations and crystal size distribution analyses, and wrote the manuscript. A.O.K. performed geostatistical investigation, drew maps, took samples and reviewed the manuscript. Y.A.P. and A.V.B. took BSE images and performed electron microscope investigations. P.M.G. drew maps. J.A.M. carried out petrographical investigations and reviewed the manuscript. V.N.Y. and N.G.K. conceived of the work, took and prepared samples. All authors discussed the manuscript.

**Conflicts of Interest:** The authors declare no conflict of interest. The founding sponsors had no role in the design of the study; in the collection, analyses or interpretation of data; in the writing of the manuscript; nor in the decision to publish the results.

## References

1. Vincent, E.A.; Phillips, R. Iron-titanium oxide minerals in layered gabbros of the Skaergaard intrusion, East Greenland. *Geochim. Cosmochim. Acta* **1954**, *6*, 1–26. [[CrossRef](#)]
2. Deer, W.A.; Howie, R.A.; Zussman, J. *Rock-Forming Minerals Volume 5 Non-Silicates*; Longmans: London, UK, 1962.
3. Turnock, A.C.; Eugster, H.P. Fe-Al Oxides: Phase Relationships below 1000 C. *J. Petrol.* **1962**, *3*, 533–565. [[CrossRef](#)]
4. Price, G.D. Subsolidus phase relations in the titanomagnetite solid solution series. *Am. Mineral.* **1981**, *66*, 751–758.
5. Sack, R.O. Spinel as petrogenetic indicators: Activity-composition relations at low pressures. *Contrib. Mineral. Petrol.* **1982**, *79*, 169–186. [[CrossRef](#)]
6. Frost, B.; Lindsley, D.; Andersen, D. Fe-Ti oxide-silicate equilibria: Assemblages with fayalitic olivine. *Am. Mineral.* **1988**, *73*, 727–740.
7. Giorso, M.S. Thermodynamic properties of hematite-ilmenite-geikielite solid solutions. *Contrib. Mineral. Petrol.* **1990**, *104*, 645–667. [[CrossRef](#)]
8. Haggerty, S.E. Oxide textures; a mini-atlas. *Rev. Mineral. Geochem.* **1991**, *25*, 129–219.
9. Frost, B.R.; Lindsley, D.H. Occurrence of iron-titanium oxides in igneous rocks. *Rev. Mineral. Geochem.* **1991**, *25*, 433–468.
10. Zhou, W.; Van der Voo, R.; Peacor, D.R.; Zhang, Y. Variable Ti-content and grain size of titanomagnetite as a function of cooling rate in very young MORB. *Earth Planet. Sci. Lett.* **2000**, *179*, 9–20. [[CrossRef](#)]
11. Hammer, J.E. Influence of fO<sub>2</sub> and cooling rate on the kinetics and energetics of Fe-rich basalt crystallization. *Earth Planet. Sci. Lett.* **2006**, *248*, 618–637. [[CrossRef](#)]
12. Ryabchikov, I.D.; Kogarko, L.N. Magnetite compositions and oxygen fugacities of the Khibina magmatic system. *Lithos* **2006**, *91*, 35–45. [[CrossRef](#)]
13. Ivanyuk, G.; Yakovenchuk, V.; Pakhomovsky, Y.; Kalashnikov, A.; Mikhailova, J.; Goryainov, P. Self-Organization of the Khibiny Alkaline Massif (Kola Peninsula, Russia). In *Earth Sciences*; Dar, I.A., Ed.; InTech: Rijeka, Croatia, 2012; pp. 131–156, ISBN 978-953-307-861-8.
14. Ondrejka, M.; Broska, I.; Uher, P. The late magmatic to subsolidus T-fO<sub>2</sub> evolution of the Lower Triassic A-type rhyolites (Silicic Superunit, Western Carpathians, Slovakia): Fe-Ti oxythermometry and petrological implications. *Acta Geol. Slovaca* **2015**, *7*, 51–61.
15. Liao, M.; Tao, Y.; Song, X.; Li, Y.; Xiong, F. Study of oxygen fugacity during magma evolution and ore genesis in the Hongge mafic-ultramafic intrusion, the Panxi region, SW China. *Acta Geochim.* **2016**, *35*, 25–42. [[CrossRef](#)]

16. Mikhailova, J.A.; Kalashnikov, A.O.; Sokharev, V.A.; Pakhomovsky, Y.A.; Konopleva, N.G.; Yakovenchuk, V.N.; Bazai, A.V.; Goryainov, P.M.; Ivanyuk, G.Y. 3D mineralogical mapping of the Kovdor phosphorite–carbonatite complex (Russia). *Miner. Depos.* **2016**, *51*, 131–149. [[CrossRef](#)]
17. Kawai, N. Exsolution of titanomagnetites and its effect on rock-magnetism III. *Proc. Jpn. Acad.* **1956**, *32*, 464–468.
18. Nagata, T. *Rock Magnetism*, 2nd ed.; Maruzen: Tokyo, Japan, 1961.
19. Akimoto, S. Magnetic properties of FeO-Fe<sub>2</sub>O<sub>3</sub>-TiO<sub>2</sub> system as a basis of rock magnetism. *J. Phys. Soc. Jpn.* **1962**, *17*, 706–710.
20. Marshall, M.; Cox, A. Magnetism of Pillow Basalts and Their Petrology. *Geol. Soc. Am. Bull.* **1971**, *82*, 537. [[CrossRef](#)]
21. Evans, M.E.; Wayman, M.L. An Investigation of the Role of Ultra-fine Titanomagnetite Intergrowths in Palaeomagnetism. *Geophys. J. Int.* **1974**, *36*, 1–10. [[CrossRef](#)]
22. Gee, J.; Kent, D.V. Magnetization of axial lavas from the southern East Pacific Rise (14°–23°S): Geochemical controls on magnetic properties. *J. Geophys. Res. Solid Earth* **1997**, *102*, 24873–24886. [[CrossRef](#)]
23. Ivanyuk, G.I.; Tyuremnov, V.A.; Balabonin, N.L. On the origin of magnetic heterogeneity of magnetites from ferroginous quartzites. *Izv. Phys. Solid Earth* **1994**, *30*, 266–272.
24. Dunlop, D.; Özdemir, Ö. *Rock Magnetism: Fundamentals and Frontiers*; Cambridge University Press: Cambridge, UK, 1997.
25. Harrison, R.J.; Putnis, A. Magnetic properties of the magnetite-spinel solid solution: Saturation magnetization and cation distributions. *Am. Mineral.* **1995**, *80*, 213–221. [[CrossRef](#)]
26. Evans, M.E.; Krása, D.; Williams, W.; Winklhofer, M. Magnetostatic interactions in a natural magnetite-ulvöspinel system. *J. Geophys. Res. Solid Earth* **2006**, *111*. [[CrossRef](#)]
27. McEnroe, S.A.; Robinson, P.; Langenhorst, F.; Frandsen, C.; Terry, M.P.; Boffa Ballaran, T. Magnetization of exsolution intergrowths of hematite and ilmenite: Mineral chemistry, phase relations, and magnetic properties of hemo-ilmenite ores with micron- to nanometer-scale lamellae from Allard Lake, Quebec. *J. Geophys. Res.* **2007**, *112*, B10103. [[CrossRef](#)]
28. Uchida, H. Single-crystal X-ray diffraction of spinels from the San Carlos Volcanic Field, Arizona: Spinel as a geothermometer. *Am. Mineral.* **2005**, *90*, 1900–1908. [[CrossRef](#)]
29. Lavina, B.; Cesare, B.; Alvarez-Valero, A.M.; Uchida, H.; Downs, R.T.; Koneva, A.; Dera, P. Closure temperatures of intracrystalline ordering in anatectic and metamorphic hercynite, Fe<sup>2+</sup>Al<sub>2</sub>O<sub>4</sub>. *Am. Mineral.* **2009**, *94*, 657–665. [[CrossRef](#)]
30. Essene, E.; Peacor, D. Crystal chemistry and petrology of coexisting galaxite and jacobsonite and other spinel solutions and solvi. *Am. Mineral.* **1983**, *68*, 449–455.
31. Bosi, F.; Skogby, H.; Fregola, R.A.; Hälenius, U. Crystal chemistry of spinels in the system MgAl<sub>2</sub>O<sub>4</sub>-MgV<sub>2</sub>O<sub>4</sub>-Mg<sub>2</sub>VO<sub>4</sub>. *Am. Mineral.* **2016**, *101*, 580–586. [[CrossRef](#)]
32. Radtke, A.S. Coulsonite, FeV<sub>2</sub>O<sub>4</sub>, a spinel-type mineral from Lovelock, Nevada. *Am. Mineral.* **1962**, *47*, 1284–1291.
33. Bosi, F.; Halenius, U.; Skogby, H. Crystal chemistry of the magnetite-ulvöspinel series. *Am. Mineral.* **2009**, *94*, 181–189. [[CrossRef](#)]
34. O’Neil, H.S.C.; Annersten, H.; Virgo, D. The temperature dependence of the cation distribution in magnesioferrite (MgFe<sub>2</sub>O<sub>4</sub>) from powder XRD structural refinements and Moessbauer spectroscopy. *Am. Mineral.* **1992**, *77*, 725–740.
35. Bosi, F.; Halenius, U.; Skogby, H. Crystal chemistry of the ulvöspinel-qandilite series. *Am. Mineral.* **2014**, *99*, 847–851. [[CrossRef](#)]
36. Nestola, F.; Ballaran, T.B.; Balic-Zunic, T.; Princivalle, F.; Secco, L.; Dal Negro, A. Comparative compressibility and structural behavior of spinel MgAl<sub>2</sub>O<sub>4</sub> at high pressures: The independency on the degree of cation order. *Am. Mineral.* **2007**, *92*, 1838–1843. [[CrossRef](#)]
37. Lucchesi, S.; Russo, U.; Della Giusta, A. Crystal chemistry and cation distribution in some Mn-rich natural and synthetic spinels. *Eur. J. Mineral.* **1996**, *9*, 31–42. [[CrossRef](#)]
38. Buddington, A.F.; Lindsley, D.H. Iron-Titanium Oxide Minerals and Synthetic Equivalents. *J. Petrol.* **1964**, *5*, 310–357. [[CrossRef](#)]
39. Tan, W.; Liu, P.; He, H.; Wang, C.Y.; Liang, X. Mineralogy and Origin of Exsolution In Ti-Rich Magnetite From Different Magmatic Fe-Ti Oxide-Bearing Intrusions. *Can. Mineral.* **2016**, *54*, 539–553. [[CrossRef](#)]

40. Ivanyuk, G.Y.; Kalashnikov, A.O.; Pakhomovsky, Y.A.; Mikhailova, J.A.; Yakovenchuk, V.N.; Konopleva, N.G.; Sokharev, V.A.; Bazai, A.V.; Goryainov, P.M. Economic minerals of the Kovdor baddeleyite-apatite-magnetite deposit, Russia: Mineralogy, spatial distribution and ore processing optimization. *Ore Geol. Rev.* **2016**, *77*, 279–311. [[CrossRef](#)]
41. Rimskaya-Korsakova, O.M. A question about regular intergrowths of spinel with magnetite. *Zap. Vsesoyuznogo Mineral. Obs.* **1950**, *89*, 178–190. (In Russian)
42. Krasnova, N.I.; Krezer, Y.L. New data on the nature of fine and ultrafine lamellae in titanomagnetite. *Eur. J. Mineral.* **1995**, *7*, 1361–1372. [[CrossRef](#)]
43. Spenser, K.J.; Lindsley, D.H. A solution model for coexisting iron-titanium oxides. *Am. Mineral.* **1981**, *66*, 1189–1201.
44. Andersen, D.J.; Lindsley, D.H. New (and final!) models for the Ti-magnetite/ilmenite geothermometer and oxygen barometer. In *Spring Meeting Eos Transactions American Geophysical Union*; American Geophysical Union: Washington, DC, USA, 1985; p. 416.
45. Lehmann, J.; Roux, J. Experimental and theoretical study of  $(\text{Fe}^{2+}, \text{Mg})(\text{Al}, \text{Fe}^{3+})_2\text{O}_4$  spinels: Activity-composition relationships, miscibility gaps, vacancy contents. *Geochim. Cosmochim. Acta* **1986**, *50*, 1765–1783. [[CrossRef](#)]
46. Mattioli, G.S.; Wood, B.J. Magnetite activities across the  $\text{MgAl}_2\text{O}_4\text{-Fe}_3\text{O}_4$  spinel join, with application to thermobarometric estimates of upper mantle oxygen fugacity. *Contrib. Mineral. Petrol.* **1988**, *98*, 148–162. [[CrossRef](#)]
47. Bacon, C.R.; Hirschmann, M.M. Mg/Mn partitioning as a test for equilibrium between coexisting Fe-Ti oxides. *Am. Mineral.* **1988**, *73*, 57–61.
48. Sack, R.O.; Ghiorso, M.S. An internally consistent model for the thermodynamic properties of Fe-Mg-titanomagnetite-aluminate spinels. *Contrib. Mineral. Petrol.* **1991**, *106*, 474–505. [[CrossRef](#)]
49. Ghiorso, M.S.; Evans, B.W. Thermodynamics of rhombohedral oxide solid solutions and a revision of the Fe-Ti two-oxide geothermometer and oxygen-barometer. *Am. J. Sci.* **2008**, *308*, 957–1039. [[CrossRef](#)]
50. Lilova, K.I.; Pearce, C.I.; Gorski, C.; Rosso, K.M.; Navrotsky, A. Thermodynamics of the magnetite-ulvospinel ( $\text{Fe}_3\text{O}_4\text{-Fe}_2\text{TiO}_4$ ) solid solution. *Am. Mineral.* **2012**, *97*, 1330–1338. [[CrossRef](#)]
51. Harrison, R.J. Thermodynamics of the R-3 to R-3c phase transition in the ilmenite-hematite solid solution. *Am. Mineral.* **2000**, *85*, 1694–1705. [[CrossRef](#)]
52. Harrison, R.J.; Redfern, S.A.T. Short- and long-range ordering in the ilmenite-hematite solid solution. *Phys. Chem. Miner.* **2001**, *28*, 399–412. [[CrossRef](#)]
53. Lattard, D.; Sauerzapf, U.; Käsemann, M. New calibration data for the Fe–Ti oxide thermo-oxybarometers from experiments in the Fe–Ti–O system at 1 bar, 1000–1300 °C and a large range of oxygen fugacities. *Contrib. Mineral. Petrol.* **2005**, *149*, 735–754. [[CrossRef](#)]
54. Ivanyuk, G.Y.; Yakovenchuk, V.N.; Pakhomovsky, Y.A. *Kovdor; Laplandia Minerals: Apatity, Russia, 2002*; ISBN 5900395413.
55. Krasnova, N.I.; Petrov, T.G.; Balaganskaya, E.G.; García, D.; Moutte, J.; Zaitsev, A.N.; Wall, F. Introduction to phoscorites: Occurrence, composition, nomenclature and petrogenesis. In *Phoscorites and Carbonatites from Mantle to Mine: The Key Example of the Kola Alkaline Province*; Zaitsev, A.N., Wall, F., Eds.; Mineralogical Society: London, UK, 2004; pp. 43–72, ISBN 0-903056-22-4.
56. Rimskaya-Korsakova, O.M. On Question about Genesis of the Kovdor Iron-Ore Deposit. In *Problems of Magmatism and Metamorphism*; Leningrad State University Publishing: Leningrad, Russia, 1963; pp. 125–142. (In Russian)
57. Kukhareno, A.A.; Orlova, M.P.; Bulakh, A.G.; Bagdasarov, E.A.; Rimskaya-Korsakova, O.M.; Nefedov, E.I.; Ilyinsky, G.A.; Sergeev, A.S.; Abakumova, N.B. *Caledonian Complex of Ultrabasic, Alkaline Rocks and Carbonatites of Kola Peninsula and Northern Karelia (Geology, Petrology, Mineralogy and Geochemistry)*; Nedra: Moscow, Russia, 1965. (In Russian)
58. Dolivo-Dobrovolsky, D.D. MINAL, Free Software. Available online: <http://www.dimadd.ru> (accessed on 8 July 2013).
59. Lepage, L.D. ILMAT: An Excel worksheet for ilmenite–magnetite geothermometry and geobarometry. *Comput. Geosci.* **2003**, *29*, 673–678. [[CrossRef](#)]
60. MELTS Fe-Ti Oxide Geothermometer. Available online: [http://melts.ofm-research.org/CORBA\\_CTserver/OxideGeothrm/OxideGeothrm.php](http://melts.ofm-research.org/CORBA_CTserver/OxideGeothrm/OxideGeothrm.php) (accessed on 16 August 2016).

61. Kalashnikov, A.O.; Ivanyuk, G.Y.; Mikhailova, J.A.; Sokharev, V.A. Approach of automatic 3D geological mapping: The case of the Kovdor phosphorite-carbonatite complex, NW Russia. *Sci. Rep.* **2017**, *7*, 6893. [[CrossRef](#)] [[PubMed](#)]
62. Zhitova, E.; Krivovichev, S.; Yakovenchuk, V.; Ivanyuk, G.; Pakhomovsky, Y.; Mikhailova, J. Crystal chemistry of natural layered double hydroxides. 4. Crystal structures and evolution of structural complexity of quintinite polytypes from the Kovdor alkaline massif, Kola peninsula, Russia. *Mineral. Mag.* **2017**. [[CrossRef](#)]
63. Randolph, A.D.; Larson, M.A. *Theory of Particulate Processes*; Academic Press: New York, NY, USA, 1971.
64. Marsh, B.D. On the Interpretation of Crystal Size Distributions in Magmatic Systems. *J. Petrol.* **1998**, *39*, 553–599. [[CrossRef](#)]
65. Clark, M.B.; Brantley, S.L.; Fisher, D.M. Power law vein thickness distribution and positive feedback in vein growth. *Geology* **1995**, *23*, 975–978. [[CrossRef](#)]
66. Mercus, H.G. *Particle Size Measurements Fundamentals, Practice, Quality*; Springer: Berlin, Germany, 2009; ISBN 9781402090158.
67. Gaydukova, V.S.; Sokolov, S.V.; Dubinchuk, V.T.; Sidorenko, G.A.; Il'yasov, A.M. About multistage decomposition of magnetite from iron ores of the Kovdor deposit. *Mineral. Zhurnal* **1984**, *6*, 64–70. (In Russian)
68. Tan, W.; He, H.; Wang, C.Y.; Dong, H.; Liang, X.; Zhu, J. Magnetite exsolution in ilmenite from the Fe-Ti oxide gabbro in the Xinjie intrusion (SW China) and sources of unusually strong remnant magnetization. *Am. Mineral.* **2016**, *101*, 2759–2767. [[CrossRef](#)]
69. Stormer, J., Jr. The effects of recalculation on estimates of temperature and oxygen fugacity from analyses of multi-component iron-titanium oxides. *Am. Mineral.* **1983**, *68*, 586–594.
70. Frost, B.R. Introduction to oxygen fugacity and its petrologic importance. *Rev. Mineral. Geochem.* **1991**, *25*, 1–9.
71. Anovitz, L.M.; Essene, E.J. Phase Equilibria in the System  $\text{CaCO}_3\text{-MgCO}_3\text{-FeCO}_3$ . *J. Petrol.* **1987**, *28*, 389–415. [[CrossRef](#)]
72. Kalashnikov, A.O.; Yakovenchuk, V.N.; Pakhomovsky, Y.A.; Bazai, A.V.; Sokharev, V.A.; Konopleva, N.G.; Mikhailova, J.A.; Goryainov, P.M.; Ivanyuk, G.Y. Scandium of the Kovdor baddeleyite–apatite–magnetite deposit (Murmansk Region, Russia): Mineralogy, spatial distribution, and potential resource. *Ore Geol. Rev.* **2016**, *72*, 532–537. [[CrossRef](#)]
73. Yund, R.A.; McCallister, R.H. Kinetics and mechanisms of exsolution. *Chem. Geol.* **1970**, *6*, 5–30. [[CrossRef](#)]
74. Putnis, A. *An Introduction to Mineral Sciences*; Cambridge University Press: Cambridge, UK, 1992.
75. Dieckmann, R.; Mason, T.O.; Hodge, J.D.; Schmalzried, H. Defects and Cation Diffusion in Magnetite (III.) Tracerdiffusion of Foreign Tracer Cations as a Function of Temperature and Oxygen Potential. *Ber. Bunsengesellschaft Phys. Chem.* **1978**, *82*, 778–783. [[CrossRef](#)]
76. Dieckmann, R.; Schmalzried, H. Defects and Cation Diffusion in Magnetite (VI): Point Defect Relaxation and Correlation in Cation Tracer Diffusion. *Ber. Bunsengesellschaft Phys. Chem.* **1986**, *90*, 564–575. [[CrossRef](#)]
77. Van Orman, J.A.; Crispin, K.L. Diffusion in Oxides. *Rev. Mineral. Geochem.* **2010**, *72*, 757–825. [[CrossRef](#)]
78. Aggarwal, S.; Dieckmann, R. Point defects and cation tracer diffusion in  $(\text{Ti}_x\text{Fe}_{1-x})_{3-\delta}\text{O}_4$  1. Non-stoichiometry and point defects. *Phys. Chem. Miner.* **2002**, *29*, 695–706. [[CrossRef](#)]
79. Eberl, D.D.; Kile, D.E.; Drits, V.A. On geological interpretations of crystal size distributions: Constant vs. proportionate growth. *Am. Mineral.* **2002**, *87*, 1235–1241. [[CrossRef](#)]
80. Myerson, A. *Handbook of Industrial Crystallization*; Butterworth-Heinemann: Oxford, UK, 2002.
81. Garside, J.; Mersmann, A.; Nyult, J. *Measurement of Crystal Growth and Nucleation Rates*, 2nd ed.; Institute of Chemical Engineers: Rugby, UK, 2002.
82. Kile, D.E.; Eberl, D.D. On the origin of size-dependent and size-independent crystal growth: Influence of advection and diffusion. *Am. Mineral.* **2003**, *88*, 1514–1521. [[CrossRef](#)]

